ELSEVIER

Phase diagram and mechanics of snap-folding of ring origami by twisting

Xiaohao Sun [a], Shuai Wu [b], Jize Dai [c], Sophie Leanza [c], Liang Yue [a], Luxia Yu [a], Yi Jin [c], H. Jerry Qi [a,*], Ruike Renee Zhao [b,*]

[a] The George W. Woodruff School of Mechanical Engineering, Georgia Institute of Technology, Atlanta, GA 30332, USA
[b] Department of Mechanical Engineering, Stanford University, Stanford, CA 94305, USA
[c] Department of Mechanical and Aerospace Engineering, The Ohio State University, Columbus, OH 43210, USA

ARTICLE INFO

ABSTRACT

Ring origami is a new strategy to design bistable foldable/deployable structures by assembling multiple rings with the same geometry. The successful folding of ring origami assembly leverages the snap-folding capability of single rings. It is thus important to model the snap-folding of ring-shaped structures for the rational design of ring origami with good foldability, stability and high areal packing ratio. This paper studies the folding mechanics of differently shaped rings (circular, elliptical, rounded rectangular and rounded triangular rings) under twisting loads by developing theoretical and three-dimensional finite element analysis (FEA) models. The rod model is re-formulated for different ring geometries as two-point boundary value problem systems, which are then solved through numerical continuation, allowing one to capture complex equilibrium paths with multiple fold points. The rod model, verified by FEA simulations and experiments, can accurately, quantitatively capture the snap-folding behaviors for rings of different geometries. Using the rod model, we analyze the folding modes in terms of foldability, stability and snapping type. Phase diagrams of folding modes are then constructed with respect to geometric parameters for the ring profile and cross-section for differently shaped rings. Diagrams of areal packing ratios are obtained using the reduced planar rod model. This work provides comprehensive mechanics insights into the ring folding through twisting and can guide future ring origami design.

1. Introduction

Origami-inspired reconfigurable structures that can be reversibly folded and deployed have enabled a variety of applications such as deployable structures (Zirbel et al., 2013; Melancon et al., 2021), reconfigurable surfaces (Dudte et al., 2016; Callens and Zadpoor, 2018), robotic arms (Martinez et al., 2012; Li et al., 2017; Wu et al., 2021), mechanical metamaterials (Silverberg et al., 2014; Filipov et al., 2015; Zhai et al., 2018; Nauroze et al., 2018) and flexible electronics (Novelino et al., 2020). One important strategy to achieve stable deploying/folding is to exploit mechanical instabilities (e.g., buckling) of slender structures (e.g., thin shells and slender rods) (Shim et al., 2012; Nasto et al., 2013; Stein-Montalvo et al., 2019; Bende et al., 2015; Liu et al., 2016; Shan et al., 2015), which enable the shape transformation between multiple stable equilibrium configurations in a self-guided manner with high tolerance of loading errors. The ring-like structures, a type of closed-loop rods, exhibit various intriguing mechanical instabilities under external loads (Yoshiaki et al., 1992) or intrinsic stimuli (Audoly and

Seffen, 2015; Bae et al., 2014; Mouthuy et al., 2012; Manning and Hoffman, 2001; Goriely and Tabor, 1997; Moulton et al., 2013; Dias and Audoly, 2014; Dias and Santangelo, 2012), showing great capabilities of shape reconfiguration. For instance, single circular rings with narrow cross-sections upon simple moment loadings (twisting or bending) can trigger the snap-through folding into stable three-covered shapes (Yoshiaki et al., 1992), exhibiting robust self-guided folding path, geometrically precise folded state and large area reduction. Such behavior has been utilized in daily life for compact storage and pop-up deploying, such as tents and car sunshades. It should be noted that similar deformations and folding behaviors of single ring-like structures can also be triggered by intrinsic planar curvature (Audoly and Seffen, 2015; Bae et al., 2014; Mouthuy et al., 2012; Manning and Hoffman, 2001), filamentary growth (Moulton et al., 2013), and curved paper folding (Dias and Audoly, 2014; Dias and Santangelo, 2012). It is also worth noting that the intrinsic twist in single or multi-covered ring structures leads to other instability modes, such as writhing and torus knots (Goriely and Tabor, 1997).

---

* Corresponding authors.
E-mail addresses: qih@me.gatech.edu (H. Jerry Qi), rrzhao@stanford.edu (R.R. Zhao).

Motivated by the folding capability of ring-like structures, Wu et al. (Wu et al., 2021) recently presented a new strategy, ring origami, for constructing foldable/deployable structures, where a 2D/3D structure is assembled by multiple rings and can be reversibly folded and deployed through buckling to achieve large area or volume change. The efficient assembling in terms of close-packing extent relies on the usage of differently shaped rings. An example is shown in Fig. 1 and Supplementary Video 1, where an assembly of six elliptical rings is first stacked into a single-ring configuration, which is folded into a stable three-covered structure with greatly reduced volume/area upon simple twisting loads. The snap-folding characteristic leads to the self-guided, robust folding path and geometrically precise folded state. The bi-stability characteristic also leads to reliable folding-deploying reversibility. However, the ring assemblies are not always foldable or stable at the folded state. The successful folding of the assembly relies strongly on the snap-folding of elementary building units (i.e., single rings), which is governed by the ring geometry (e.g., overall profile and cross-section). The ring geometry also impacts the areal packing ratio due to the snap-folding. These imply the importance of the rational design of geometries for ring origami and thus motivate the need of theoretically modeling the snap-folding mechanics of ring-shaped structures, in particular their foldability and stability. Although finite element analysis (FEA) models have been used to study the folding behaviors of different rings (Wu et al., 2021), the high computational cost of three-dimensional (3D) FEA makes it difficult to acquire comprehensive insights into the ring folding mechanics, e.g., to construct complete phase diagrams for foldability, stability and areal packing ratio. In addition, 3D FEA in the previous study is not sufficient to capture different snapping instabilities (e.g., snap-back) (Crisfield, 1981; Crisfield, 1986), thus providing relatively limited mechanics insights. Given the high slenderness of ring structures, reduced-order theories (e.g., rod model) are desirable to further understand the snap-folding mechanics, identify key parameters controlling the ring folding, and guide the design of ring origami.
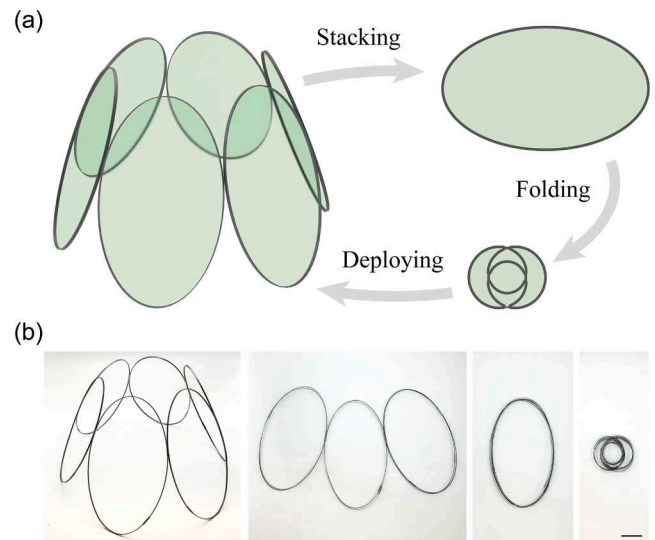

Fig. 1. Ring origami: folding of ring assembly through buckling. (a) Schematic and (b) experiment of folding an elliptical ring assembly. Scale bar: 5 cm.

Audoly, 2014; Dias and Santangelo, 2012). In addition, rod-based structures with other geometries or topologies exhibit abundant mechanical instabilities under various loading conditions, such as perversion in telephone cords or tendrils (Goriely and Tabor, 1998) and coiling of DNA molecules (Fuller, 1978). Examples of studies utilizing rod models for these intriguing behaviors include those on various types of buckling behaviors under different mechanical loads (O'Reilly, 2017; Healey and Mehta, 2005; Sano and Wada, 2019; Yu and Hanna, 2019), coiling or perversion under bi-strip strain mismatch or intrinsic curvatures (Goriely and Tabor, 1998; McMillen, 2002; Haijun and Zhong-can, 1998; Huang et al., 2012; Liu et al., 2014; Wang et al., 2020), writhing under intrinsic twist (Goriely and Tabor, 2000; Goriely et al., 2001),

Supplementary Video 1.
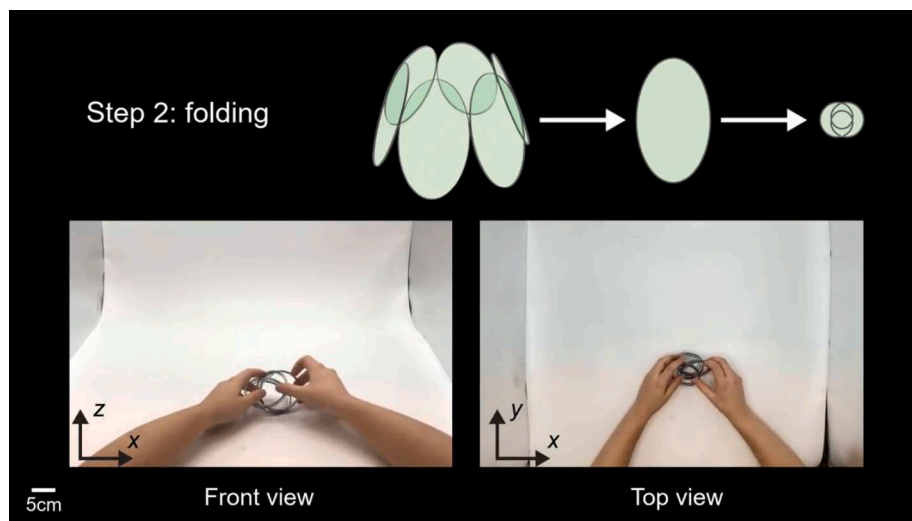
The classical Kirchhoff rod theory (Love, 2013; O'Reilly, 2017), which can describe the geometrically nonlinear deformations of rod structures in 3D space, has been widely used to model mechanical behaviors of rod-like or ring-like objects (Yoshiaki et al., 1992; Audoly and Seffen, 2015; Bae et al., 2014; Mouthuy et al., 2012; Manning and Hoffman, 2001; Goriely and Tabor, 1997; Moulton et al., 2013; Dias and

morphogenesis due to filamentary growth (Moulton et al., 2013; Lessinnes et al., 2017; Moulton et al., 2020), shapes of Mobius strips (Mahadevan and Keller, 1993; Moore and Healey, 2019), mechanics of knots (Jawed et al., 2015; Patil et al., 2020); hard-magnetic elastica (Wang et al., 2020; Wang et al., 2021), and multi-rod structures such as lattices (Weeger et al., 2018), fabrics (Weeger et al., 2017), gridshells (Baek and Reis, 2019; Baek et al., 2018) and bigons (Yu et al., 2021).

In this work, we develop a Kirchhoff rod-based theoretical model to study the twisting-induced snap-folding behaviors of differently shaped ring structures (circular, elliptical, rounded rectangular and rounded triangular rings) and investigate how the geometric parameters of rings affect the foldability and stability of the ring twisting process. Note that although the bending loads can also induce the snap-folding, this study focuses on the twisting since it is a simpler and more efficient loading approach in practice (Wu et al., 2021). In Section 2, we first introduce the classical Kirchhoff rod equations and present boundary conditions for the simplest case, i.e., twisting of circular rings, which poses a two-point boundary value problem (BVP). Next, we re-formulate the governing equations and boundary conditions for other shaped rings to obtain two-point BVPs such that they can be readily implemented into general-purpose numerical continuation packages. We then introduce the numerical solution method. In addition, 3D FEA models are presented for the twisting process of different rings to verify the theoretical model. Section 3 presents the results for different ring types. For each ring type, using the rod model, we identify various folding modes in terms of foldability, stability and snapping type, based on which we construct phase diagrams of folding modes with respect to geometric parameters for the ring profile and cross-section. Then, reduced planar rod models are developed to rapidly capture the folded shapes and construct diagrams of areal packing ratios. Section 4 summarizes the work and gives general mechanics insights into the controlling factors for the folding modes and areal packing ratios for the twisting of different rings.

2. Model and methods

2.1. Theoretical model

2.1.1. Circular ring: Kirchhoff rod

We model the ring structures as inextensible, unshearable Kirchhoff rods (Love, 2013). The Kirchhoff rod model is introduced in Appendix A.1. The governing equations given by Eq. (A.15) are a system of thirteen first-order ODEs with respect to the arc length s of the centerline of a rod. Briefly, Eq. (A.15)$_{1-6}$ describe the balance of force $\mathbf{F}$ and moment $\mathbf{M}$ (equilibrium) where linear constitutive relations between the $\mathbf{M}$ and the *Darboux vector* $\mathbf{k}$ (defining the curvature) have been implied, Eq. (A.15)$_{7-10}$ represent the kinematic relations for the local orientations $(\mathbf{d}_1, \mathbf{d}_2, \mathbf{d}_3)$ of the rod cross-section (rotational), Eq. (A.15)$_{11-13}$ represent the kinematic relation for the position vector $\mathbf{r}$ of the rod centerline (translational).

Boundary conditions for the twisting of circular rings are given in Appendix A.2, where the 1/4 model is considered. The quaternion description of rotations is adopted, thus the rotational boundary conditions are first expressed in Euler angles and then converted into quaternion components (q_0, q_1, q_2, q_3) using Eq. (A.24) (see Appendix A.3). The ODEs, together with the boundary conditions, can be readily used for a rod of (i) single-segment, i.e., a rod segment for which all dependent variables in ODEs are continuous, and with (ii) explicit forms of the natural curvature $k_1^{(u)}(s)$ and its s-derivative, such as circular rings under twisting loads.

For either elliptical rings which have no explicit form $k_1^{(u)}(s)$ or multi-segment rings (such as rounded rectangular and triangular rings) which have multiple discontinuities in $k_1^{(u)}(s)$ over the entire ring, the governing equations will be re-formulated and boundary conditions be given in the following two subsections.

2.1.2. Elliptical ring: re-formulation

Note in Eq. (A.15)$_{4-6}$ (i.e., momentum-balance equations) that the natural curvature $k_1^{(u)}$ and its s-derivative cannot be expressed as explicit

functions of the arc length s, therefore we seek to re-parameterize the governing equations. Let a denote the length of the semi-horizontal axis ($\mathbf{E}_3$-axis, see Fig. A.1c), $b = ca$ the length of the semi-vertical axis ($\mathbf{E}_2$-axis), c the aspect ratio. The centerline of a natural elliptical ring can be parameterized as $\mathbf{r} = (0, ca\cos\tau, a\sin\tau)$ in the global basis ($\mathbf{E}_1, \mathbf{E}_2, \mathbf{E}_3$) (see Fig. A.1c). Then $k_1^{(u)}$ and its τ-derivative can be given as analytical functions of τ, i.e.,

$$\overline{k}_1^{(u)} = k_1^{(u)}a = \frac{c}{\left(\sqrt{c^2(\sin\tau)^2 + (\cos\tau)^2}\right)^3}$$

$$\frac{d\overline{k}_1^{(u)}}{d\tau} = \frac{3c(1-c^2)\cos\tau\sin\tau}{\left(\sqrt{c^2(\sin\tau)^2 + (\cos\tau)^2}\right)^5} \tag{1}$$

Here, the bars are included to distinguish dimensionless and dimensional variables, and the reference length $L = a$ has been used for the normalization in Eq. (A.14), such that $\overline{k}_1^{(u)} = k_1^{(u)}a$. From Eq. (1), it is easy to write the initial curvatures at the boundaries (e.g., $\overline{k}_1^{(u)}(0) = 1/c^2$). Further, the τ-derivative of any relevant variables can be obtained using the s-derivative and the chain rule, i.e.,

$$\frac{d(\cdot)}{d\tau} = \frac{d(\cdot)}{d\overline{s}}\frac{d\overline{s}}{d\tau} = \frac{d(\cdot)}{d\overline{s}}\sqrt{c^2(\sin\tau)^2 + (\cos\tau)^2} \tag{2}$$

Applying Eq. (2) can re-formulate Eq. (A.15) as thirteen first-order ODEs with respect to the parameter τ. Here we give the momentum-balance equations as examples,

$$\frac{d\overline{k}_1}{d\tau} = \frac{d\overline{k}_1^{(u)}}{d\tau} + \left[\frac{1}{a}\overline{F}_2 + \left(\frac{\beta}{\alpha} - 1\right)\overline{k}_2\overline{k}_3\right]\sqrt{c^2(\sin\tau)^2 + (\cos\tau)^2}$$

$$\frac{d\overline{k}_2}{d\tau} = \left[-\frac{1}{\beta}\overline{F}_1 - \left(\frac{\alpha}{\beta} - 1\right)\overline{k}_1\overline{k}_3 + \frac{\alpha}{\beta}\overline{k}_1^{(u)}\overline{k}_3\right]\sqrt{c^2(\sin\tau)^2 + (\cos\tau)^2} \tag{3}$$

$$\frac{d\overline{k}_3}{d\tau} = \left[(\alpha - \beta)\overline{k}_1\overline{k}_2 - \alpha\overline{k}_1^{(u)}\overline{k}_2\right]\sqrt{c^2(\sin\tau)^2 + (\cos\tau)^2}$$

where $\overline{k}_1^{(u)}$ is given by Eq. (1). Note that the independent variable τ is then treated as the fourteenth dependent variable (whose τ-derivative $\equiv$ 1) to achieve an autonomous ODE system for easier numerical implementation.

With the re-formulated system, we again consider the 1/4 model. Let the reference length L be a, the parameter τ is in $[0, \pi/2]$, then the boundary conditions at $\tau = 0$ and $\tau = \pi/2$ follow exactly those of the circular rings (BC-I and BC-II of Fig. A.1c).

2.1.3. Multi-segment rings: Augmented system

For a rod with multiple connected segments, such as rounded rectangular and triangular rings, the natural curvature $k_1^{(u)}$ is discontinuous at the joints. Thus a multi-point BVP has to be considered. To facilitate the numerical implementation, we formulate the multi-point BVP as a two-point BVP using an approach as detailed below. The approach is similar to that used in Yu et al. (2021) and Ascher et al. (1995). We introduce a vector composed of components of all relevant variables, $\mathbf{u} = (F_1, F_2, F_3, k_1, k_2, k_3, q_0, q_1, q_2, q_3, r_1, r_2, r_3)$, where (F_1, F_2, F_3) and (k_1, k_2, k_3) are components of $\mathbf{F}$ and $\mathbf{k}$ in the local basis $(\mathbf{d}_1, \mathbf{d}_2, \mathbf{d}_3)$, respectively, (r_1, r_2, r_3) are components of $\mathbf{r}$ in the global basis ($\mathbf{E}_1, \mathbf{E}_2, \mathbf{E}_3$). Thus Eq. (A.15) can be written as $\mathbf{u}' = \mathbf{g}(\mathbf{u}, k_1^{(u)}, \alpha, \beta)$ where α and β are dimensionless parameters given in Eq. (A.16). Then the governing equations for a rod with n connected segments can be augmented as follows,

$$\frac{d}{d\underline{s}}\left(\mathbf{u}^{(1)}, \mathbf{u}^{(2)}, ..., \mathbf{u}^{(n)}\right) = \left(\frac{L_0^{(1)}}{L}\mathbf{g}\left(\mathbf{u}^{(1)}, k_1^{(u)(1)}\right), \frac{L_0^{(2)}}{L}\mathbf{g}\left(\mathbf{u}^{(2)}, k_1^{(u)(2)}\right), ..., \frac{L_0^{(n)}}{L}\mathbf{g}\left(\mathbf{u}^{(n)}, k_1^{(u)(n)}\right)\right) \tag{4}$$

where $(\cdot)^{(i)}$ represent the corresponding variable or function ($\bullet$) for the i-th segment; α, β are omitted since they are identical for different segments of a ring; the chain rule $d(\cdot)/d\underline{s} = d(\cdot)/d\bar{s} \cdot d\bar{s}/d\underline{s}$ has been used for each segment to re-formulate the $s^{(i)}$-derivative in Eq. (A.15), where $s^{(i)} \in [0, L_0^{(i)}/L]$ is dimensionless segment arc length (with $L_0^{(i)}$ being segment length and L an identical reference length), as the $\underline{s}$-derivative in Eq. (4), where $\underline{s} \in [0, 1]$ is a unified arc length for all different segments. For rounded rectangular or triangular rings considered in our study, a segment is either circular or straight. L is set to be the radius of the rounded fillet, denoted as r; therefore the coefficient $L_0^{(i)}/L$ is equal to the angle change $\theta^{(i)}$ of i-th segment. After augmentation, for a rod with n connected segments, the complete ODE system (Eq. (4)) consists of $13n$ unknowns and $13n$ first-order differential equations with respect to one independent variable (i.e., $\underline{s}$), thus requiring $13n$ boundary conditions to well-pose a two-point BVP system.

For rounded rectangular rings, we consider the 1/4 model. The boundary conditions for $\mathbf{u}^{(1)}(\underline{s} = 0)$ and $\mathbf{u}^{(n)}(\underline{s} = 1)$ follow Eqs.(A.17), (A.18) and Eqs.(A.19), (A.20) described in Appendix A.2 (BC-I and BC-II of Fig. A.1c), respectively, which yields 13 boundary conditions. In addition, at each joint, the equilibrium and geometric compatibility imply 12 continuous conditions for F_1, F_2, F_3, k_2, k_3, q_0, q_1, q_2, q_3, r_1, r_2, r_3 and one jump condition for k_1. These conditions at all joints can be formulated as mixed boundary conditions which couple the certain variables at two ends $\underline{s} = 0$ and $\underline{s} = 1$, providing additional $13(n\text{-}1)$ boundary conditions. The two-point BVP system is thus well-posed.

For rounded triangular rings (limited to the isosceles case), we will use the 1/2 model due to the reduced symmetry. Opposite twisting loads are applied around the axis of symmetry of the ring. In this case, twisting angles are prescribed for $\mathbf{u}^{(1)}(\underline{s} = 0)$ and $\mathbf{u}^{(n)}(\underline{s} = 1)$, which follow BC-III and BC-II of Fig. A.1c, respectively. Equations for BC-III can be given in a similar way to that for BC-II (Appendix A.2). This would give 14 boundary conditions, one more than expected. Similar to the circular rings (with 1/4 model) discussed in Appendix A.2, the condition $|\mathbf{q}|=1$ ($\mathbf{q}$ is the quternion vector, see Appendix A.3) is implied by Eq. (A.15)$_{7\text{-}10}$ and the prescription of four quaternion components for either $\underline{s} = 0$ at segment 1 or $\underline{s} = 1$ at segment n. Therefore, we specify four q_i values for one end but only three q_i values for the other end, obtaining 13 boundary conditions for $\mathbf{u}^{(1)}(\underline{s} = 0)$ and $\mathbf{u}^{(n)}(\underline{s} = 1)$. The remaining $13(n\text{-}1)$ boundary conditions are specified at all segment joints.

2.1.4. Numerical solution method

The well-posed two-point BVP system is numerically solved using the numerical continuation package, Continuation Core and Toolboxes (COCO) (Dankowicz and Schilder, 2013; Dankowicz and Schilder, 2010), operated in MATLAB (2020a, MathWorks, Natick, MA). The BVP system is discretized using the orthogonal collocation method to yield a system of algebraic equations. COCO combines a continuation algorithm and a Newton iteration method (Dankowicz and Schilder, 2010) to solve the problem. We choose the twisting angle γ as the only continuation parameter. The solution starts from the initial ring configuration ($\gamma = 0$) and is continued along a solution path as γ varies. In each step, the dependent variables and γ are solved simultaneously. The continuation is terminated once γ reaches π, representing the completion of a simple twisting process. COCO (Dankowicz and Schilder, 2013) can identify singular points such as fold points (also referred to as snapping points or limit points) and branch points (Weinitschke, 1985; Eriksson et al., 1999), where the instabilities would occur, and trace the solutions on one or multiple branches. In the absence of branch points (this is the case

in our study), the numerical continuation yields a single solution path with varying γ, which allows us to extract an equilibrium curve for twisting moment versus γ. There may arise two types of snapping instabilities, snap-through and snap-back (Crisfield, 1981; Crisfield, 1986), which can be identified from the equilibrium curves. Generally, the former refers to the snapping behaviors that occur under the moment ("load")-control, while the latter refers to those under the angle ("displacement")-control. The fold points can be classified accordingly. For the ring twisting, the cases with snap-back must also involve the snap-through feature; therefore such cases will be identified as the snap-back scenario.

Note that when computing the phase diagram, we perform continuation on single parameter γ, instead of on others such as (α, β) or $(h/t, \nu)$ and other relevant geometric parameters, since the direct continuation on latter parameters does not represent a physically realistic process and may not yield correct foldability/stability behaviors.

2.2. Finite element model

To verify the rod theory, finite-element analysis (FEA) of the ring folding process is performed with the commercial software ABAQUS (2018, Simulia, Providence, RI), following our previous study (Wu et al., 2021). Linear elastic model is utilized with Young's modulus of 1.8 GPa and Poisson's ratio of 0.3 to represent the polymer used for ring fabrication. The 3D geometry is meshed with linear brick elements with reduced integration (C3D8R in ABAQUS element library). Mesh convergence study of circular rings is carried out to ensure the mesh independence of FEA prediction. The ring folding is induced by twisting two ends of the ring in reverse directions through an angle-controlled process. During the snap-folding, the two ends rotate and are free to translate along the twisting axis (Fig. A.1c). A small damping factor, which provides a negligible amount of dissipated energy, is used to stabilize the ring buckling simulations. The reaction moment-twisting angle curves and folding configurations of rings are exported to compare with the rod-model predictions. Since our focus is the influence of the geometry and dimension on the folding, the self-contact of the ring during folding is not considered for both theoretical model and FEA simulations.

2.3. Experiments

The 6-ring assembly presented in Fig. 1 is fabricated by joining adjacent elliptical rings with tape. Stainless steel strips of rectangular cross-section (0.50 mm thickness, 2.0 mm height) are manually shaped to form the elliptical rings, with $b/a = 0.6$. All the plastic rings with different geometries and cross-section properties presented in the results section are prepared by filling a UV curable polymer resin into predesigned polydimethylsiloxane molds (PDMS) (Sylgard 184, DowCorning Inc., USA), followed by a two-step curing process, i.e., UV curing for one minute and a post thermal curing at 80 °C for 10 min. The UV curable resin contains isobornyl acrylate (Sigma Aldrich, USA) and tricyclodecanedimethanol diacrylate (Sigma Aldrich) with a weight ratio of 80:20. 1 wt% photoinitiator (Irgacure 819, Sigma Aldrich) is added for free radical polymerization. In addition, 0.01 wt% fluorescent dye (Solvent green 5, Orichem International Ltd., China) is used for light fluorescence. Uniaxial tensile tests of the cured resin are performed, showing a Young's modulus of 1.8 GPa.

3. Results and discussions

Comparing to our previous study (Wu et al., 2021), results obtained from the rod model will be mainly presented, focusing on the phase diagrams of folding modes (foldability, stability and snapping type) and areal packing ratios and the resulting new insights into the folding mechanics for differently shaped rings. Comparisons with previous results (FEA and experiments) will also be given for the validation of the rod model and completeness of the result presentation.

We see from Eq. (A.15) that the ring folding is governed by the rod's bending-to-torsional rigidity ratios α and β, which are functions of Poisson's ratio ν and h/t for rectangular cross-sections (Eq. (A.16)). The non-circular rings are governed by additional parameters that describe the ring shape (see Eqs. (3) and (4)). Due to the inextensible, unshearable assumption, the folding is not affected by the ratio of overall to cross-sectional dimensions. We therefore fix $\nu = 0.3$ and the overall dimension to thickness ratio specific to each ring shape and focus on studying how the cross-section (h/t) and ring profile geometries affect the folding behavior.

3.1. Circular ring

We first consider the case of circular rings to gain initial insights into the ring folding process. Fig. 2a illustrates the geometry of the ring, where R denotes the radius, h and t denote the height (out-of-plane) and thickness (in-plane) of the cross-section, respectively. $R/t = 200$ is

adopted in the FEA model and experiments. Using the rod model, we construct a solution manifold in the 3D parametric space from the calculated moment (MR/GJ)-angle (γ) curves for different h/t values (Fig. 2b). Curves with representative h/t values are highlighted against the FEA results. The deformed shapes during the twisting are also compared with the FEA and experiment (Fig. 2c). Excellent agreements are achieved in both the curves and deformed shapes, except the discrepancy due to the self-contact.

Four folding modes with respect to h/t are identified from the curves: un-foldable ($h/t < 1.51$), unstable folding with snap-back ($1.51 \leq h/t < 1.84$), unstable folding with snap-through only ($1.84 \leq h/t < 3.48$) and stable folding with snap-through only ($h/t \geq 3.48$). The folded rings are in the planar three-covered state regardless of h/t, corresponding to the areal packing ratio of $1/9$. These are further discussed as follows.

Foldability is determined by the twisting moment at $\gamma = \pi$. The folded ring is in a pure bending state (e.g., $h/t = 4$, Fig. 2c), implying that $M(\gamma = \pi) = 0$ (Appendix B); whilst the un-foldable ring involves the combined bending and twisting (e.g., $h/t = 1$, Fig. 2c), thus $M(\gamma = \pi) > 0$. Note that the three-covered shape is always an equilibrium solution, e. g., for $h/t = 1$ (Fig. C.1, Appendix C.1), such solution can be attained by the further continuation of γ, which, however, is neither accessible nor stable under the simple twisting. Therefore, such cases are identified as un-foldable cases.

Stability is determined by the moment–angle slope at $\gamma = \pi$. The negative slope implies that the removal of external loading would cause the ring to deploy. This corresponds to a local maximum in the strain
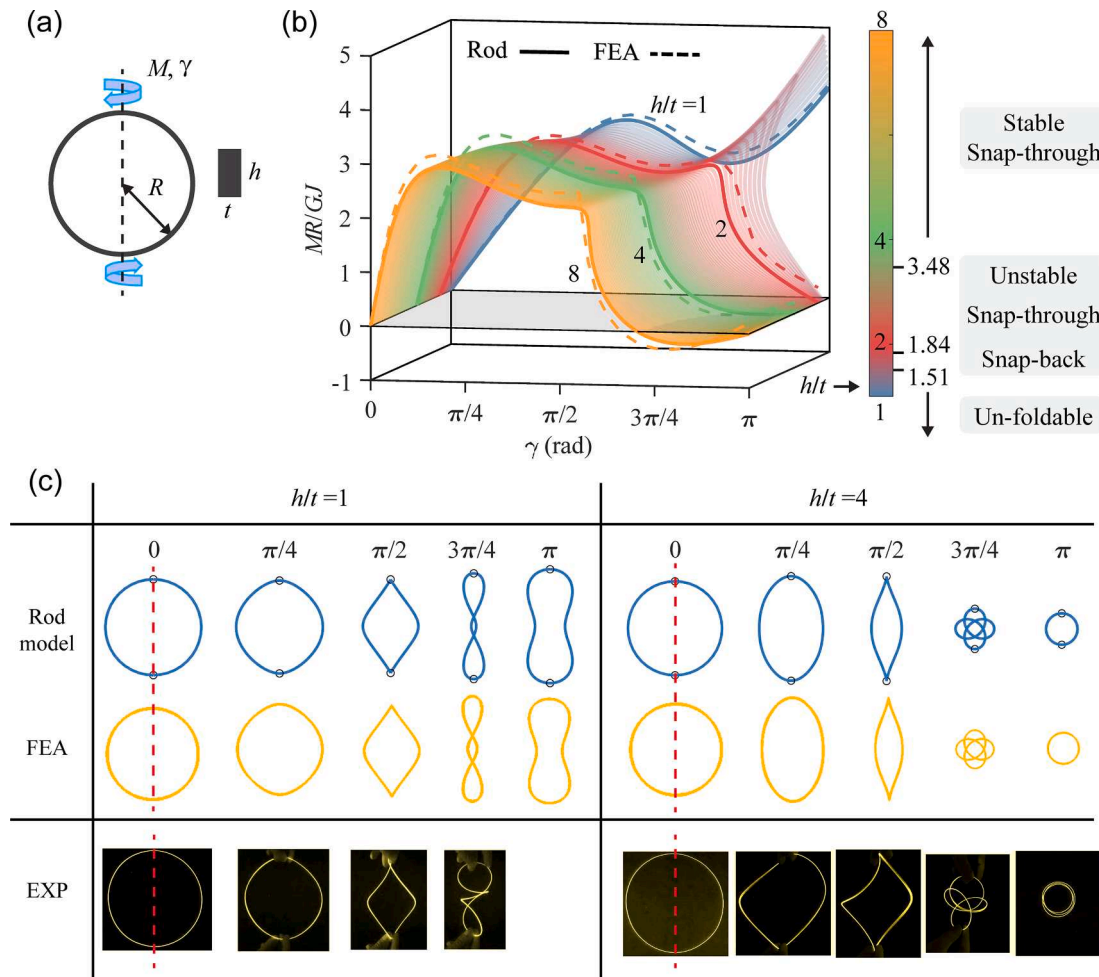

Fig. 2. Folding of circular rings. (a) Schematic of ring geometry and applied twisting load. (b) Relations between the normalized applied moment MR/GJ and twisting angle γ predicted by the rod theory (solid lines) and FEA (dashed lines) for different h/t values. (c) Rod-model, FEA and experimental folding processes (snapshots of deformed shapes at different γ values) of circular rings for cases with $h/t = 1$ (left) and 4 (right).

energy-angle plot (see $h/t = 2$ in Fig. C.2, Appendix C.2). In contrast, the positive moment-angle slope at $\gamma = \pi$ represents a local minimum of strain energy (see $h/t = 4$ or 8 in Fig. C.2), and the folded configuration can hence maintain stably. The stable folding for $h/t = 4$ is validated by the experiments (Fig. 2c).

We further analyze the snapping type for the foldable cases. The snap-through (or non-monotonic moment–angle relation) can be seen for all the cases in Fig. 2b, implying the structural buckling. We further identify the snap-back (snapping that occurs under the angle control) instability, which is present for a small range of h/t. In a practical hand-folding process (the moment and angle cannot be accurately prescribed), the foldable rings will snap to the folded configuration in a self-guided manner after the snapping points.

Increasing h/t promotes the foldability and stability. Intuitively, the twisting loads induce the combined bending (k_1, k_2) and twisting (k_3) in the ring; the successful folding relies on the preference for in-plane bending (k_1) to trigger appropriate buckling. For $h/t = 1$, there is no preferred bending direction. Increasing h/t leads to more dominating in-plane bending (k_1), thus making it easier to trigger the snap-folding. This principle applies to all the ring shapes to be studied.

3.2. Elliptical rings

Next, we consider the case of elliptical rings. Fig. 3a illustrates the geometry of the ring. Without loss of generality, let a and b denote the lengths for the semi-major axis (or y-axis) and semi-minor axis (or x-axis), respectively ($a > b$); h and t are the same as before. The $a/t = 200$ is adopted in the FEA model and experiments. Relevant geometric parameters include the elliptical profile aspect ratio b/a (which describes the ring narrowness), cross-sectional aspect ratio h/t and the twisting axis. Ma/GJ is used as the dimensionless moment.

Using the rod model, we construct a phase diagram of foldability, stability and snapping type in the parametric space of b/a ($0.5 \sim 1$) and h/t ($0 \sim 4$) from the calculated moment–angle relationships (Fig. 3a). Diagrams for the x-axis and y-axis twisting are joined together at the $b/a = 1$ (circular ring) boundary. Five regions are identified: un-foldable, unstable folding with snap-through only, unstable folding with snap-back, stable folding with snap-through only, and stable folding with snap-back. Although the un-foldable case may also involve snapping, the snapping type is identified only for foldable cases. The marked symbols in Fig. 3a are representative cases whose moment–angle curves and/or ring shapes during the twisting by the rod model are compared with those by the FEA and experiments in Fig. 2 ($b/a = 1$, circular ring, different h/t), Fig. 4 ($b/a = 0.6$, different h/t and twisting axes) and Fig. D.1 ($h/t = 4$, different b/a and twisting axes, Appendix D.1). Excellent agreements among the rod model, FEA and experiments validate the rod model. Next, we discuss the insights acquired from the phase diagram.

First, increasing h/t generally promotes the foldability and stability. As h/t increases, a transition from un-foldable to unstable folding and
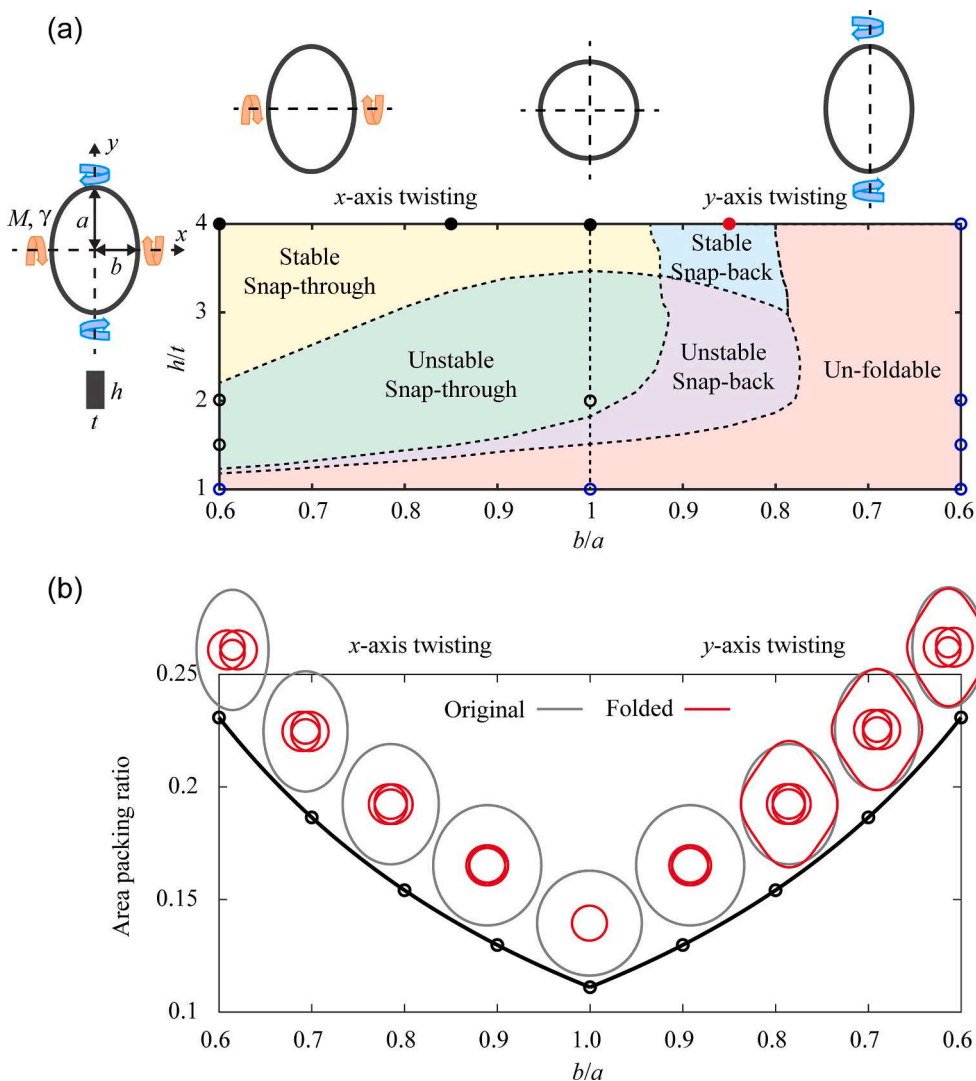

Fig. 3. Elliptical ring folding through twisting. (a) Phase diagram for the folding modes of elliptical rings with respect to b/a, h/t and the twisting axis. Snapping type is identified for foldable cases only. The marked symbols are representative cases whose moment–angle curves are provided in Fig. 2 ($b/a = 1$, different h/t), Fig. 4 ($b/a = 0.6$, different h/t and twisting axes), Fig. D.1 ($h/t = 4$, different b/a and twisting axes) (b) Areal packing ratios of folded elliptical rings versus b/a obtained using the planar rod model (Appendix B). For representative b/a values, the planar rod model-predicted folded shapes as well as the final shapes of the ring twisting ($\gamma = \pi$, $h/t = 4$) are provided.

then to stable folding is present (Fig. 3a). The transition in moment–angle curve can be seen in an example case of $b/a = 0.6$, x-axis twisting (Fig. 4b left).

Second, the rings with relatively small b/a (<0.78) and the y-axis (long-axis) twisting are always un-foldable (Fig. 3a; see curves for the example case of $b/a = 0.6$ in Fig. 4b right). Indeed, the x-axis (short-axis) twisting thus exhibits superior foldability (i.e., greater phase zone) than that of the y-axis (long-axis) case (Fig. 3a). Intuitively, this is because the change of moment-arm length influences the combination of bending (k_1, k_2) and twisting (k_3) deformations.

Third, the stability boundaries for the x-axis and y-axis twisting are nearly identical (i.e., symmetric to the $b/a = 1$ axis), both showing increased stability (i.e., more inside the stable zone, possessing higher moment-angle slope at $\gamma = \pi$ and thus resisting more fluctuation in loadings or geometries) with reduced b/a (increased narrowness) (Fig. 3a). The nearly identical stability boundary for the two twisting axes is expected because they possess the identical folded shape and very similar deploying deformation mode. We, therefore, infer that the stability boundary within the y-axis twisting, un-foldable region (the folded ring may be achieved through complex loadings) is also identical to that with the x-axis twisting.

Fourth, regarding the snapping type, the snap-through dominates in the x-axis twisting while the snap-back mainly falls in the y-axis twisting (Fig. 3a). The equilibrium moment–angle curve (solid line) for an example case with snap-back ($h/t = 4$, $b/a = 0.85$, y-axis twisting) is shown in Fig. D.1b, which well captures the two snapping points of the angle-controlled FEA curves (dashed) during loading and unloading and

the resulting hysteresis behavior. In short, the stability of a folded elliptical ring is affected by the ring profile (b/a) and the cross-section (h/t) but not by the twisting axis; the foldability and snapping type are affected by all the three factors (Fig. 3a).

Finally, the folded ring shape depends only on the ring profile (b/a) and not on the other two factors (although they affect the foldability); all the successfully folded rings are at the three-covered state ($\int_0^{L_0} k_1 ds = 6\pi$). To better guide the design of ring origami, we study the areal packing ratios for different b/a values. Since the rings may be un-foldable under simple twisting, instead of only using the ring-twisting model for the folded shapes, we present a reduced planar rod model (Appendix B) that can rapidly capture the folded shapes to construct the relationship between the areal packing ratio and b/a (Fig. 3b). For representative b/a values, the folded shapes calculated by the reduced model, as well as the final shapes by the ring twisting ($\gamma = \pi$, $h/t = 4$), are shown as insets (Fig. 3b). For the foldable rings under simple twisting, the final shapes are consistent with those by the reduced model; for the un-foldable rings, the final shapes are not at the folded (three-covered) states. In addition, decreasing b/a (increasing narrowness) can increase the areal packing ratio; the lowest packing ratio is 1/9, achieved by the circular rings ($b/a = 1.0$).

3.3. Rounded rectangular rings

We consider the case with rounded rectangular rings. Fig. 5a illustrates the geometry of the ring. Let a and b denote the lengths for the
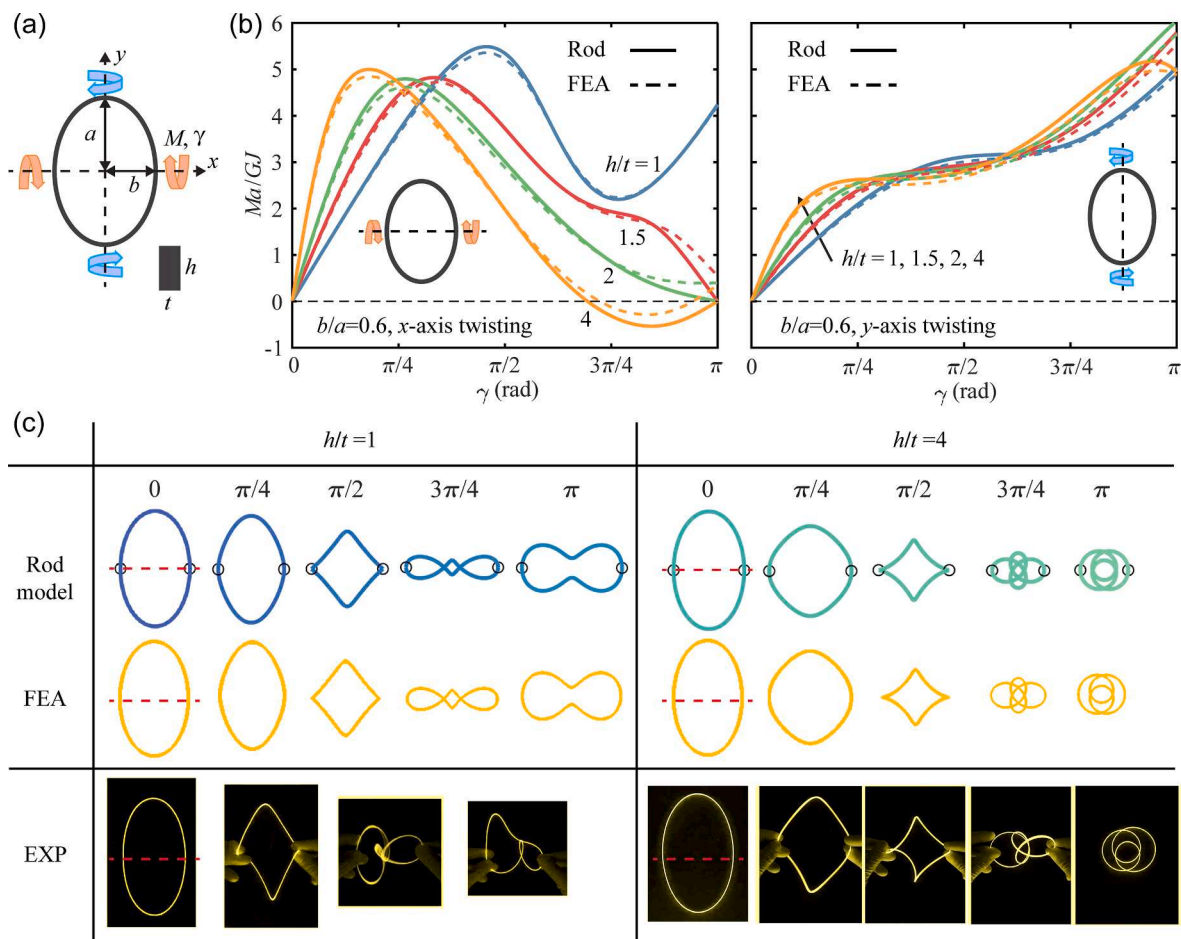

Fig. 4. Elliptical ring folding through twisting. (a) Schematic of ring geometry and applied twisting load. (b) Normalized twisting moment Ma/GJ versus angle γ curves obtained using rod theory (solid lines) and FEA (dashed lines) for fixed $b/a = 0.6$ and different h/t values and twisting axes (left: x-axis; right: y-axis). (c) Rod-model, FEA and experimental folding processes through the x-axis twisting for $h/t = 1$ (left) and 4 (right).
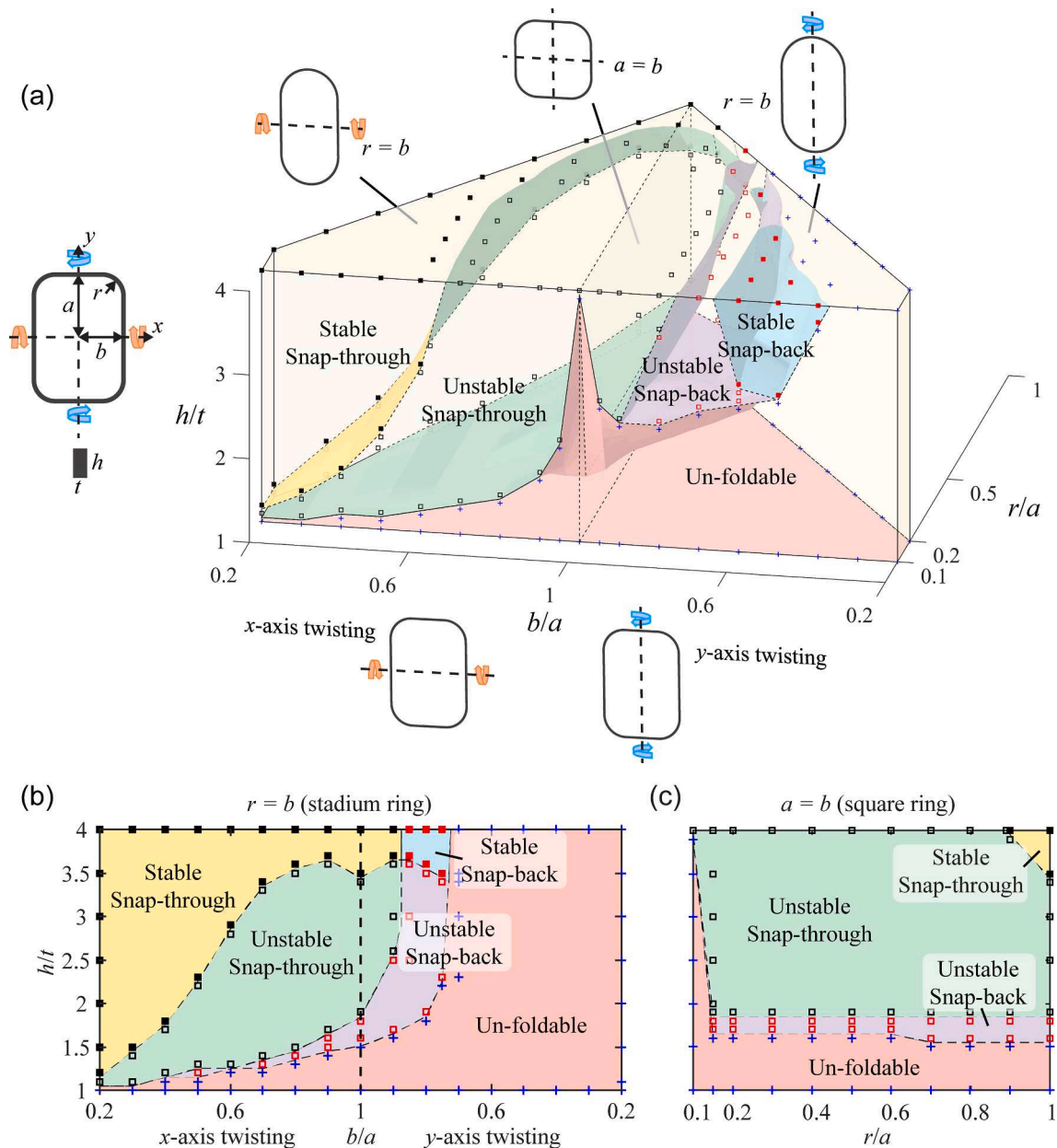
Fig. 5. Folding of rounded rectangular rings through twisting. (a) Three-dimensional phase diagram for the folding modes of rounded rectangular rings with respect to the geometric parameters b/a, r/a and h/t, and the twisting axis. Five regions are identified: un-foldable, unstable folding with snap-through, unstable folding with snap-back, stable folding with snap-through, and stable folding with snap-back. (b)-(c) Two-dimensional phase diagrams for (b) $r = b$ and (c) $a = b$.

semi-major axis (or y-axis) and semi-minor axis (or x-axis), respectively; r is the radius of rounded fillets; h and t are the same as before. The $a/t = 200$ is adopted in the FEA and experiments. Relevant geometric parameters include b/a (which describes the narrowness), relative fillet radius r/a (which describes the sharpness), h/t and the twisting axis. Ma/GJ is used as the dimensionless applied moment.

Using the rod model, we construct a 3D phase diagram of the foldability, stability and snapping type in the parametric space of b/a ($0.2 \sim 1$), r/a ($0.1 \sim 1$) and h/t ($1 \sim 4$) from the calculated moment–angle relationships (Fig. 5a). Diagrams for the x-axis and y-axis twisting are joined together at the $b/a = 1$ (rounded square ring) boundary. Note that the condition $r/a \leq b/a$ must be met, so the phase diagram occupies a prismatic space. Five phases are identified and separated by multiple boundary surfaces. For better visualization, we give two 2D phase diagrams sliced from the 3D diagram for two special rectangular rings, i.e., the stadium ring ($r = b$, Fig. 5b) and the square ring ($a = b$, Fig. 5c),

respectively. The cases used to determine the phase boundaries are marked in three diagrams. To better guide the design, we further construct a 2D contour diagram of the areal packing ratio of the folded rings with respect to the b/a and r/a (Fig. 6) using an analytical formula Eq. (B.8) derived from the reduced planar rod model (Appendix B). For representative b/a and r/a values, the folded shapes by Eq. (B.8) and the final shapes by the x-axis twisting ($\gamma = \pi$, $h/t = 4$), as displayed together in Fig. 6, are exactly overlapped.

In addition, for some representative geometric parameters, the moment–angle curves and/or ring shapes during the twisting by the rod model are compared with those by the FEA and experiments, as shown in Fig. 7 ($r/a = 0.3$, $b/a = 0.6$, different h/t and twisting axes) and Fig. D.2 ($r/a = 0.3$, $h/t = 4$, different b/a and twisting axes, Appendix D.2). Excellent agreements are achieved among the rod model, FEA and experiments, except the discrepancy in the ring shapes due to self-contact (e.g., Fig. 7c). Next, we discuss the insights acquired from the phase
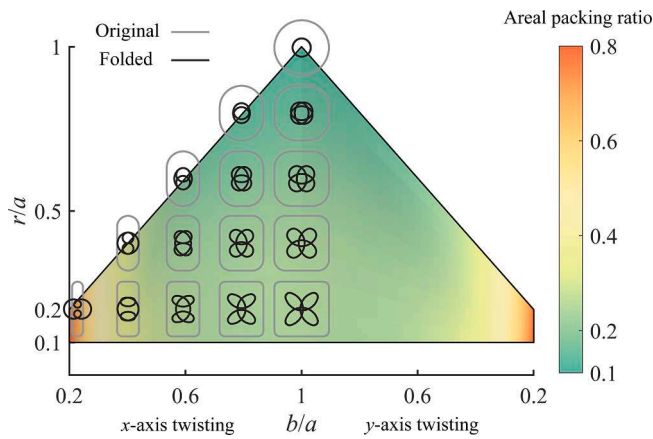
Fig. 6. Areal packing ratios of the folded rounded rectangular rings versus b/a and r/a obtained using Eq. (B.8) (Appendix B). The folded shapes by Eq. (B.8) and the final shapes by the ring twisting ($\gamma = \pi$, $h/t = 4$, x-axis) for representative cases are provided.

diagram and the areal packing ratio diagram, supplemented by results from the representative cases.

First, increasing h/t generally promotes the foldability and the folded ring's stability (Fig. 5a-5c). As an example, for $r/a = 0.3$ and $b/a = 0.6$,

the ring exhibits a transition from un-foldable to stable folding as h/t increases for both twisting axes (Fig. 7b).

Second, due to the geometric similarity, the elliptical ring and rounded rectangular ring exhibit some similar physical features. For example, reducing b/a (increasing narrowness) promotes the stability under the x-axis twisting but tends to diminish the foldability under the y-axis twisting (Fig. 5a and 5b; see Fig. D.2b for example). The x-axis (short-axis) twisting thus exhibits superior foldability and stability (i.e., greater phase zones) than that of the y-axis (long-axis) twisting. Although the stability boundaries should be identical for the two axes, the reduced foldability under the y-axis twisting leads to isolated, smaller phases regions for the stable folding (e.g., $b/a \approx 0.6$, $r/a < 0.4$, $h/t > 3.0$). Indeed, for the stadium ring, the nearly identical stability boundaries for the two twisting axes as well as a great similarity in the entire phase diagram to the elliptical ring can be seen (Fig. 5b).

Third, the rectangular ring also exhibits similar snapping features to the elliptical ring. The snap-through dominates in the x-axis twisting regardless of b/a while transitioning to the snap-back in the y-axis twisting as b/a decreases (narrowness increases) (Fig. 5a and b). An example case with snap-back ($r/a = 0.3$, $b/a = 0.6$, $h/t = 4$, y-axis twisting) is shown in Fig. 7b, where the two snapping points and hysteresis present in the FEA (angle control) loading–unloading curves are well captured by the theoretical equilibrium curve. For the square ring ($b/a = 1$), the unstable folding with snap-through dominates the foldable region (Fig. 5c; see Fig. D.2b for the curves with $h/t = 4$ and
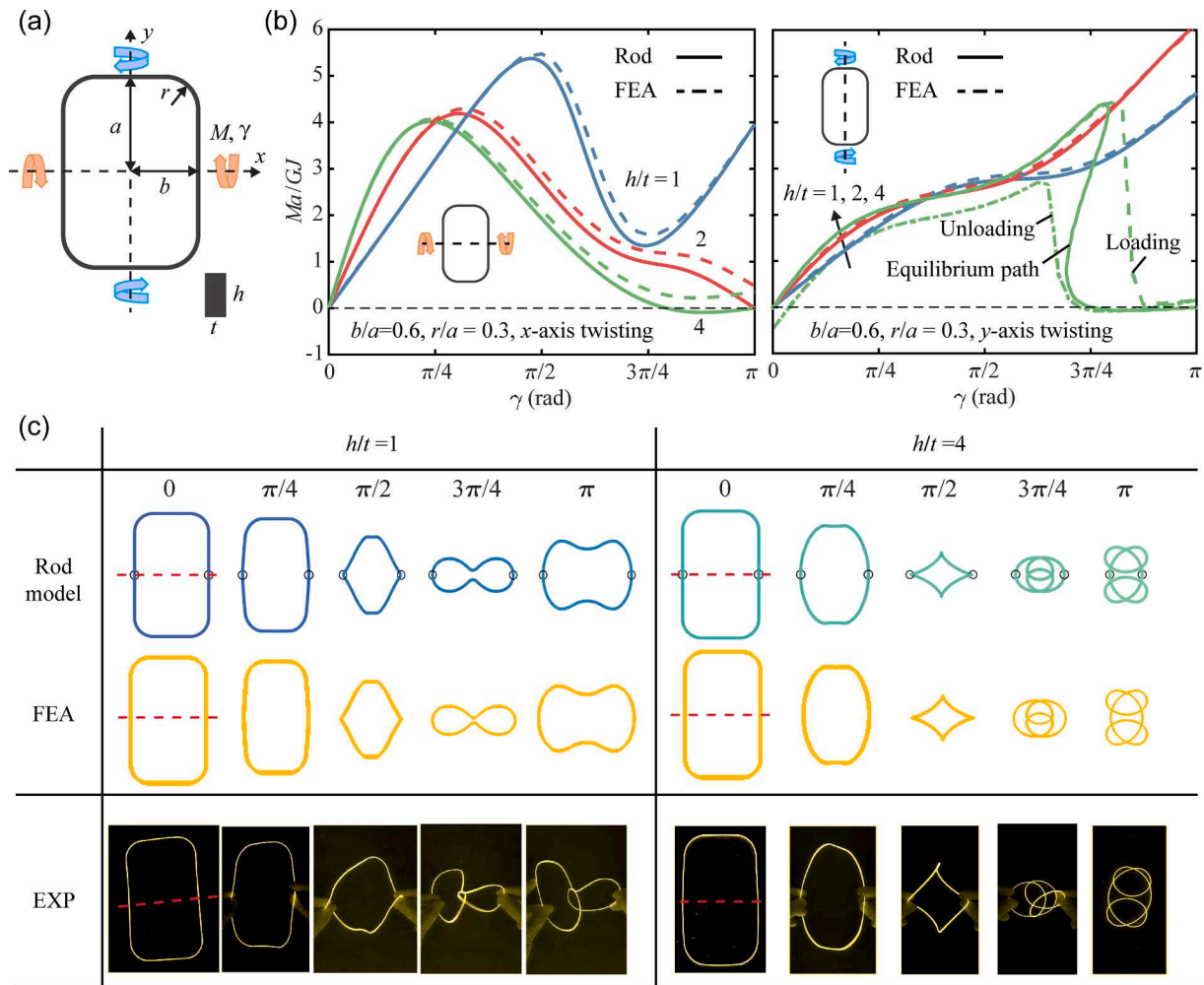

Fig. 7. Folding of rounded rectangular rings through twisting. (a) Schematic of ring geometry and applied twisting load. (b) Normalized twisting moment Ma/GJ versus angle γ curves obtained using rod theory (solid lines) and FEA (dashed lines) for $b/a = 0.6$, $r/a = 0.3$ and different h/t values and twisting axes (left: x-axis; right: y-axis). (c) Rod-model, FEA and experimental folding processes through the x-axis twisting for $h/t = 1$ (left) and 4 (right).

different *r/a* values).

Fourth, the fillet size *r/a* has insignificant effects on the foldability and stability (Fig. 5a and c; see Fig. D.2b for example), but a very sharp square ring (*r/a* = 0.1 or below) is un-foldable (Fig. 5c).

Finally, in summary, the stability of a folded ring is affected by the ring profile (*b/a* and *r/a*) and the cross-section (*h/t*) but not very sensitive to the twisting axis; the foldability and snapping type are affected by the three factors (Fig. 5a); the folded shapes depend on the *b/a* and *r/a* but not on the other two factors, and are always in the three-covered state (Fig. 6). In addition, decreasing *b/a* (increasing narrowness) and *r/a* (increasing sharpness) can increase the areal packing ratio. The lowest packing ratio (1/9) is achieved by the circular rings (*b/a* = *r/a* = 1.0) and the highest ratio (0.80) by the narrowest (*b/a* = 0.2) rectangular ring. The very sharp (*r/a* = 0.1) square ring can still achieve a low packing ratio (0.24).

3.4. Rounded triangular ring

Finally, we consider the case with rounded isosceles triangular rings. Fig. 8a illustrates the geometry of the ring, where α_T is the vertex angle, *a* is the base length, *r* is the radius of rounded fillets, and *h* and *t* are the same as before. The *a/t* = 600 is adopted in the FEA and experiments. Relevant geometric parameters include the α_T, *r/a* (describing the sharpness) and *h/t*. *Ma/GJ* is used as the dimensionless applied moment.

Using the rod model, we construct a 3D phase diagram of the foldability, stability and snapping type with respect to α_T (30° ~ 120°), *r/a* (0.033 ~ 0.384) and *h/t* (1 ~ 4) (Fig. 8a). The constraint $r \leq R_C$ must be satisfied, where R_c denotes the radius of the ring's inscribed circle,
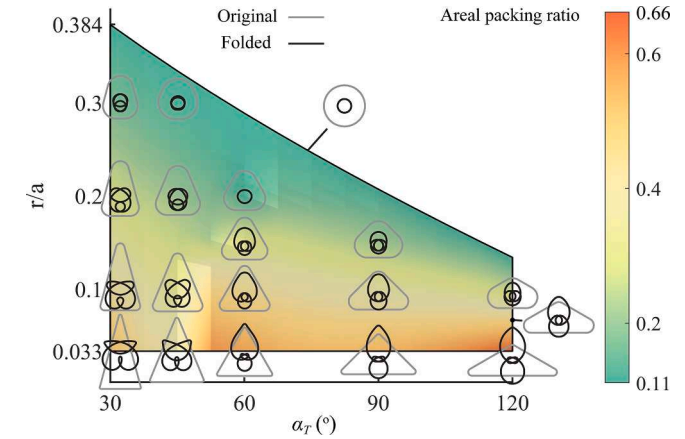

Fig. 9. Areal packing ratio of the folded rounded triangular rings with respect to geometric parameters. The folded shapes for representative α_T and *r/a* values are provided.

$$R_C = \frac{a}{2}\tan\left(\frac{\pi}{4} - \frac{\alpha_T}{4}\right) \tag{5}$$

The phase diagram thus occupies a prismatic space. The $r = R_C$ implies a circular ring. Five phases are identified and separated by multiple boundary surfaces. For better visualization, we give two 2D phase diagrams sliced from the 3D diagram for two special triangular rings with $\alpha_T = 60°$ (Fig. 8b) and $\alpha_T = 120°$ (Fig. 8c), respectively. The cases used to determine the phase boundaries are marked in three diagrams. To better guide the design, we further construct a 2D contour diagram of the areal
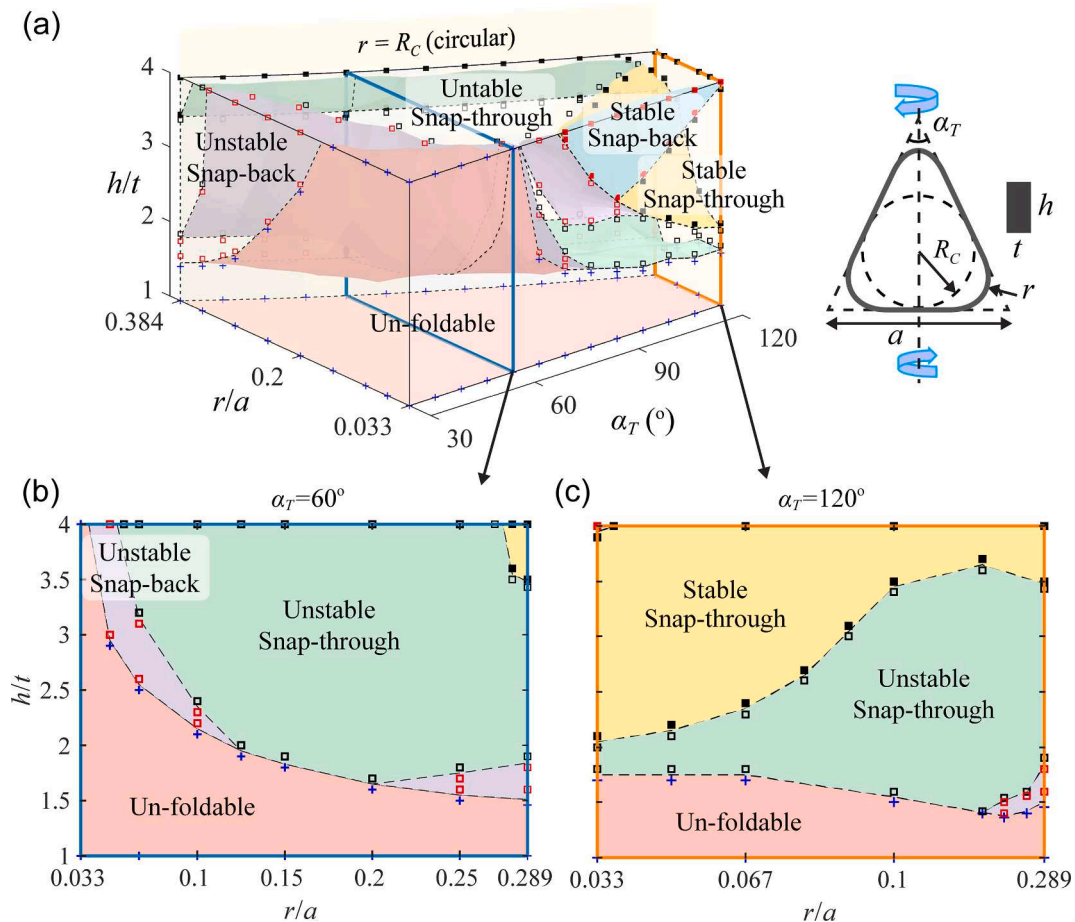

Fig. 8. Folding of rounded triangular rings through twisting. (a) Three-dimensional phase diagram for the folding modes of rounded triangular rings with respect to the geometric parameters α_T, *r/a* and *h/t*. Five regions are identified: un-foldable, unstable folding with snap-through, unstable folding with snap-back, stable folding with snap-through, and stable folding with snap-back. (b)-(c) Two-dimensional phase diagrams for (b) $\alpha_T = \pi/3$ and (c) $\alpha_T = 2\pi/3$.
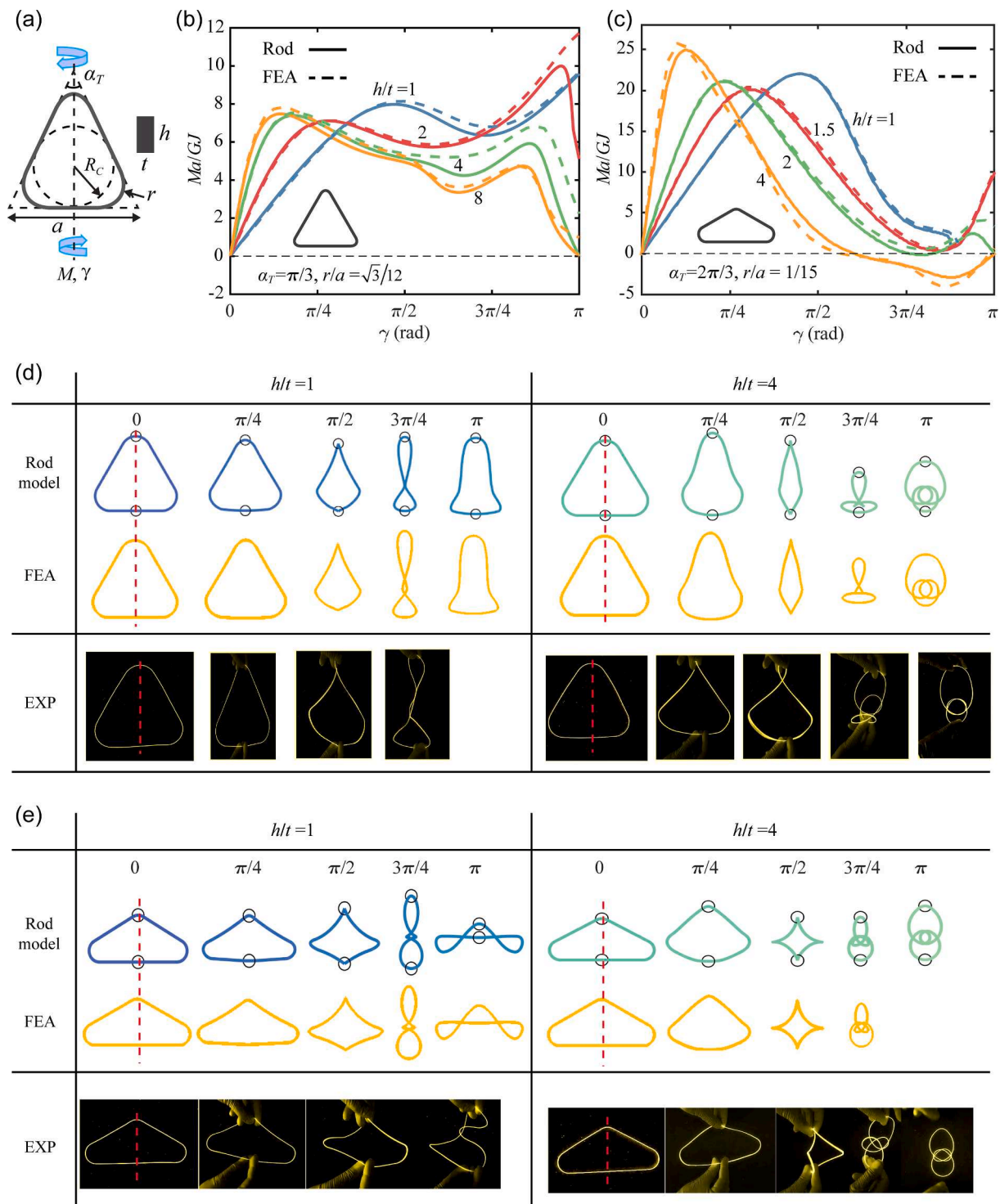
Fig. 10. Folding of rounded triangular rings through twisting. (a) Schematic of ring geometry and applied twisting load. (b), (c) Relations between the normalized applied moment Ma/GJ and twisting angle γ predicted by rod model (solid lines) and FEA (dashed lines) for different geometries. The r/a value is adjusted according to α_T such that $r/R_C = 1/2$. (b) $\alpha_T = \pi/3$ (equilateral), $r/a = \sqrt{3}/12$ (≈ 0.144) and different h/t values. (c) $\alpha_T = 2\pi/3$, $r/a = 1/15$ and different h/t values. The $h/t = 1$ case shows a very complex equilibrium curve, which is truncated at $\gamma = 7\pi/8$ for clearer displaying. The complete curve is shown in Fig. 11a. (d), (e) Rod-model, FEA and experimental folding processes of triangular rings for cases with $h/t = 1$ (left) and 4 (right). (d) $\alpha_T = \pi/3$. (e) $\alpha_T = 2\pi/3$.

packing ratio of the folded rings with respect to the α_T and r/a (Fig. 9). The folded shapes for representative α_T and r/a values are also shown.

In addition, for some representative geometric parameters, the moment–angle curves and/or ring shapes during the twisting by the rod model are compared with those by the FEA and experiments, as shown in Fig. 10, Fig. 11 and Fig. D.3. Excellent agreements are achieved among

the rod model, FEA and experiments, except the discrepancy in the ring shapes due to self-contact. Next, we discuss the insights acquired from the phase diagram and the areal packing ratio diagram, supplemented by results from these representative cases.

First, the general principle that increasing h/t promotes the foldability and stability still holds true in a large parametric space (Fig. 8a–c;
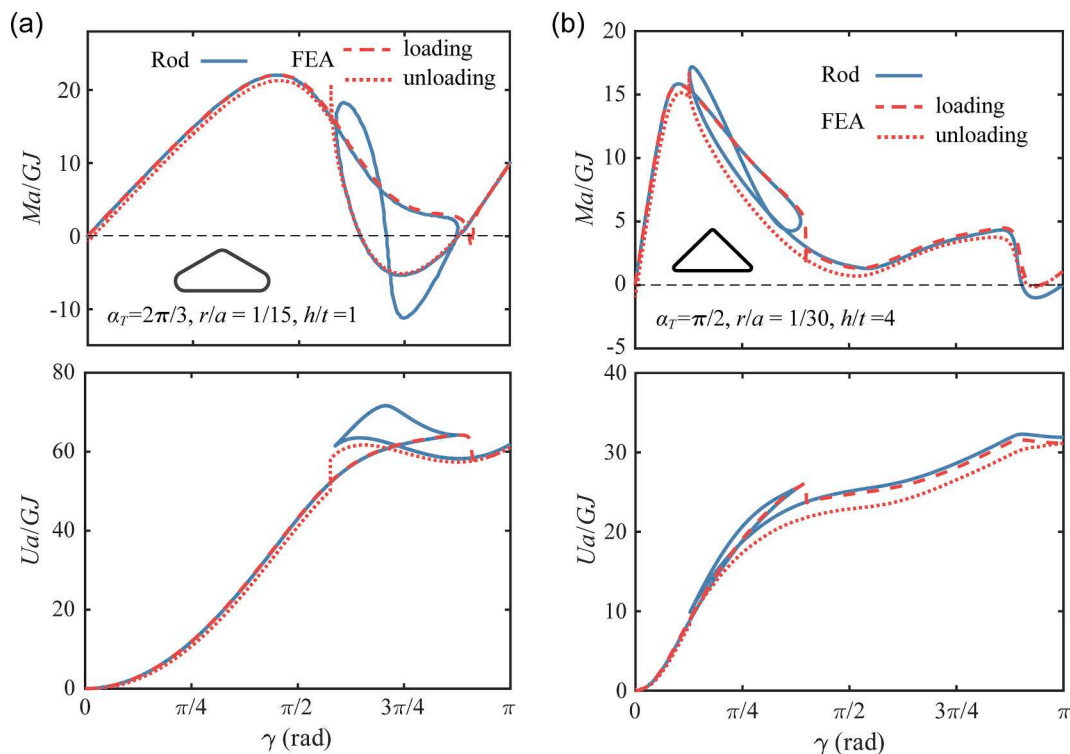
Fig. 11. Folding of rounded triangular rings through twisting. Moment-angle and strain energy-angle relations for cases with snap-back instabilities: (a) un-foldable case, $\alpha_T = 2\pi/3$, $r/a = 1/15$, $h/t = 1$ and (b) stable folding case, $\alpha_T = \pi/2$, $r/a = 1/30$, $h/t = 4$. The rod-model predicted equilibrium curves (solid lines), as well as the FEA-predicted loading (dashed lines) and unloading (dotted lines) curves, are provided. U is the strain energy and Ua/GJ is used as the dimensionless energy.

see Fig. 10b and c for examples of the transition in the moment–angle curve as h/t changes).

Second, the ring with vertex angle α_T in [75°, 120°] shows superior foldability and stability (i.e., greater phase zones) than that with α_T in [30°, 75°] (Fig. 8a; see Fig. D.3a for the transition in the moment–angle curve as α_T changes). Reducing the fillet size r/a (increasing sharpness) would diminish foldability for the smaller α_T range (e.g., $\alpha_T = 60°$, Fig. 8b), but affects little on the foldability and could even significantly promote the stability for the larger α_T range (e.g., $\alpha_T = 120°$, Fig. 8c; see Fig. D.3b for the transition in the moment–angle curve as r/a changes). Note that reducing r/a can also complicate the equilibrium path (see Fig. D.3 and Fig. 11).

Third, the foldable region is dominated by unstable folding (Fig. 8a and 8b). The stable folding is only achieved in nearly circular rings ($r/a \approx R_C$) or relatively sharp ($r/a < R_C/2$) rings with obtuse α_T (e.g., $\alpha_T = 120°$, Fig. 8c). Most stable folding cases are dominated by snap-through, while using very small fillet size ($r/a \leq 0.033$) could lead to snap-back instabilities and very complex equilibrium paths. Fig. 11a and b show examples for the un-foldable and stable folding cases, respectively. For either case, the FEA (angle control) curve follows the theoretical curve but snaps at different points during loading and unloading. A certain segment of theoretical curve is un-accessible within the snap-back region. Also, the strain energy curve shows the loss in strain energy when the solution snaps, which is dissipated by ABAQUS to accommodate the snapping.

Finally, in summary, the foldability, the folded ring's stability, and the snapping type are affected by all the geometric parameters: the ring profile (α_T and r/a) and the cross-section (h/t) (Fig. 8a). The folded ring shapes depend on α_T and r/a but not on the h/t value; all the successfully folded rings are at the three-covered state (Fig. 9). In addition, increasing α_T and decreasing r/a (increasing sharpness) can increase the areal packing ratio. The lowest packing ratio (1/9) is achieved for the circular rings ($r/R_C = 1.0$) and the highest ratio (0.66) by the sharpest ($r/a = 0.033$) obtuse triangular ring ($\alpha_T = 120°$). Interestingly, the

equilateral ($\alpha_T = 60°$) triangular rings with $r/a = 0.2$ can achieve a very low packing ratio (0.12).

4. Conclusions

We present a theoretical, computational and experimental study on the snap-folding mechanics of differently shaped rings (circular, elliptical, rounded rectangular and rounded triangular rings) under twisting loads. We first present a theoretical model for the ring folding problem using the Kirchhoff rods (inextensible and unshearable) and formulate the twisting of different rings into two-point BVP systems. The equations for the Kirchhoff rods are re-formulated for elliptical rings and are augmented for the multi-segment rings. The two-point BVPs are then solved through numerical continuation, yielding equilibrium solution paths for the ring twisting process. In addition, we develop 3D FEA models for twisting of different rings. The reduced planar rod models are presented to rapidly capture the folded configurations. Using the two models, we study the folding mechanics of differently shaped rings. For all the cases, the rod model predicts quantitatively consistent folding behaviors with the FEA simulations and the experiments. Three folding modes in terms of foldability and stability (i.e., un-foldable, stable folding and unstable folding) are identified from the moment–angle curves by the rod model. For the foldable cases, two snapping modes, i.e., snap-through and snap-back, are further identified. We then construct the phase diagrams for different rings, describing these folding modes (i.e., foldability, stability and snapping type) with respect to relevant geometric parameters (cross-section and ring profile parameters).

Generally, applying simple twisting loads can only achieve the three-covered folded states; increasing the cross-sectional aspect ratio h/t promotes the foldability and the folded ring's stability for all the different rings. The elliptical and rounded rectangular rings exhibit qualitatively similar behaviors: the stability is not affected by the twisting axis, which tends to be promoted with the increasing narrowness (decreasing b/a); whilst the foldability tends to be promoted for the

x-axis twisting but to be diminished for the *y*-axis twisting with the increasing narrowness; the snap-through dominates in the *x*-axis twisting while the snap-back becomes more significant in the *y*-axis case. For triangular rings, using the obtuse rather than acute vertex angle α_T generally promotes foldability and stability. The unstable folding dominates; the stable folding is only achieved in highly rounded (i.e., nearly circular) rings or relatively sharp ($r/a < R_C/2$) rings with obtuse α_T; most stable folding cases are dominated by snap-through.

Finally, we study the folded configurations and areal packing ratios for different rings. Diagrams of areal packing ratios with respect to relevant geometric parameters are obtained using the reduced planar rod model. The lowest areal packing ratio (1/9) is achieved for circular rings. Increasing the narrowness (elliptical and rectangular rings) or reducing the roundness (rectangular and triangular rings) generally increase the packing ratio (i.e., less compacted).

The areal packing ratio diagrams, together with the phase diagrams of folding modes, can guide the design of ring origami. Although this study only focuses on the snap-folding under twisting loads, our approach can be used to model the bending- or intrinsic curvature-induced folding process of differently shaped rings, which have alternative deforming paths. This will be studied in the future.

Declaration of Competing Interest

The authors declare that they have no known competing financial interests or personal relationships that could have appeared to influence the work reported in this paper.

Acknowledgements

Appendix A. Theoretical model for twisting of rings

A.1. Kirchhoff rod model

In this section, we briefly summarize the theory of Kirchhoff rods (Love, 2013). An inextensible and unshearable rod is considered. As shown in Fig. A.1a, the centerline of the rod is described by a position vector $\mathbf{r}(s)$, where $s \in [0, L_0]$ is the arc length and L_0 is the total length of the rod segment, which does not change due to the inextensible assumption. A local orthonormal director basis, $(\mathbf{d}_1(s), \mathbf{d}_2(s), \mathbf{d}_3(s))$, attached to the centerline can be defined, where $\mathbf{d}_3(s)$ is the unit tangent vector of the centerline,

$$\mathbf{d}_3 = \mathbf{r}'(s) \tag{A1}$$

with $(\bullet)' = d(\bullet)/ds$ here and in what follows. The $\mathbf{d}_1(s)$ and $\mathbf{d}_2(s)$ are two orthonormal unit vectors representing the principal orientations of a rod cross-section at s, which remain perpendicular to $\mathbf{d}_3(s)$ due to the unshearable assumption; the basis satisfies the right-handed convention (i.e., $\mathbf{d}_3 = \mathbf{d}_1 \times \mathbf{d}_2$). The kinematic description for rotating of the local basis is given by

$$\mathbf{d}'_i(s) = \mathbf{k} \times \mathbf{d}_i(s), \quad i = 1, 2, 3 \tag{A2}$$

where $\mathbf{k} = k_1\mathbf{d}_1 + k_2\mathbf{d}_2 + k_3\mathbf{d}_3$ is the *Darboux vector*, whose first two components k_1 and k_2 in the local basis represent the bending curvatures associated with the frame rotation around $\mathbf{d}_1$ and $\mathbf{d}_2$ as s changes, and the third component k_3 represents the twisting density, a metric of frame rotation around $\mathbf{d}_3$. To facilitate understanding, an alternative matrix form of Eq. (A.2) can be written as

$$\frac{d}{ds} \begin{Bmatrix} \mathbf{d}_1 \\ \mathbf{d}_2 \\ \mathbf{d}_3 \end{Bmatrix} = \begin{pmatrix} 0 & k_3 & -k_2 \\ -k_3 & 0 & k_1 \\ k_2 & -k_1 & 0 \end{pmatrix} \begin{Bmatrix} \mathbf{d}_1 \\ \mathbf{d}_2 \\ \mathbf{d}_3 \end{Bmatrix} = [\mathbf{K}] \begin{Bmatrix} \mathbf{d}_1 \\ \mathbf{d}_2 \\ \mathbf{d}_3 \end{Bmatrix} \tag{A3}$$

In Kirchhoff rod theory, the stress acting on the cross-section at $\mathbf{r}(s)$ gives rise to a resultant force $\mathbf{F}(s)$ and resultant moment $\mathbf{M}(s)$ attached to the centerline. The balance for linear and angular momentum in terms of $\mathbf{F}$ and $\mathbf{M}$, upon dropping the inertial effects yields the static equilibrium equations.

$$\begin{aligned} \mathbf{F}' + \mathbf{f} &= \mathbf{0} \\ \mathbf{M}' + \mathbf{r}' \times \mathbf{F} + \mathbf{m} &= \mathbf{0} \end{aligned} \tag{A4}$$

where $\mathbf{f}$ and $\mathbf{m}$ are the body force and couple per length. Here, we assume $\mathbf{f} = \mathbf{0}$ and $\mathbf{m} = \mathbf{0}$ since no gravity, self-contact or other distributed loads are considered. Then, with the help of Eq. (A.3), projecting Eq. (A.4) along the local basis $(\mathbf{d}_1, \mathbf{d}_2, \mathbf{d}_3)$ yields six scalar equations for equilibrium,

$$F'_1 - F_2k_3 + F_3k_2 = 0, \quad F'_2 - F_3k_1 + F_1k_3 = 0, \quad F'_3 - F_1k_2 + F_2k_1 = 0 \tag{A5}$$

$$M'_1 - M_2k_3 + M_3k_2 - F_2 = 0, \quad M'_2 + M_1k_3 - M_3k_1 + F_1 = 0, \quad M'_3 - M_1k_2 + M_2k_1 \tag{A6}$$

where F_i and M_i are components of $\mathbf{F}$ and $\mathbf{M}$ in the local basis. Eqs. (A.5) to (A.6) represent the local forms for the balance of forces and moments at static equilibrium.

Linear constitutive relation is used to further modify the equilibrium equations. We use $\mathbf{k}^{(u)}$, the unstressed *Darboux vector*, to define the natural shape of the rod. Then the deformation ($\mathbf{k}-\mathbf{k}^{(u)}$) is related to the resultant moment $\mathbf{M}$ of a cross-section through

$$\mathbf{M} = EI_1\left(k_1 - k_1^{(u)}\right)\mathbf{d}_1 + EI_2\left(k_2 - k_2^{(u)}\right)\mathbf{d}_2 + GJ\left(k_3 - k_3^{(u)}\right)\mathbf{d}_3 \tag{A7}$$
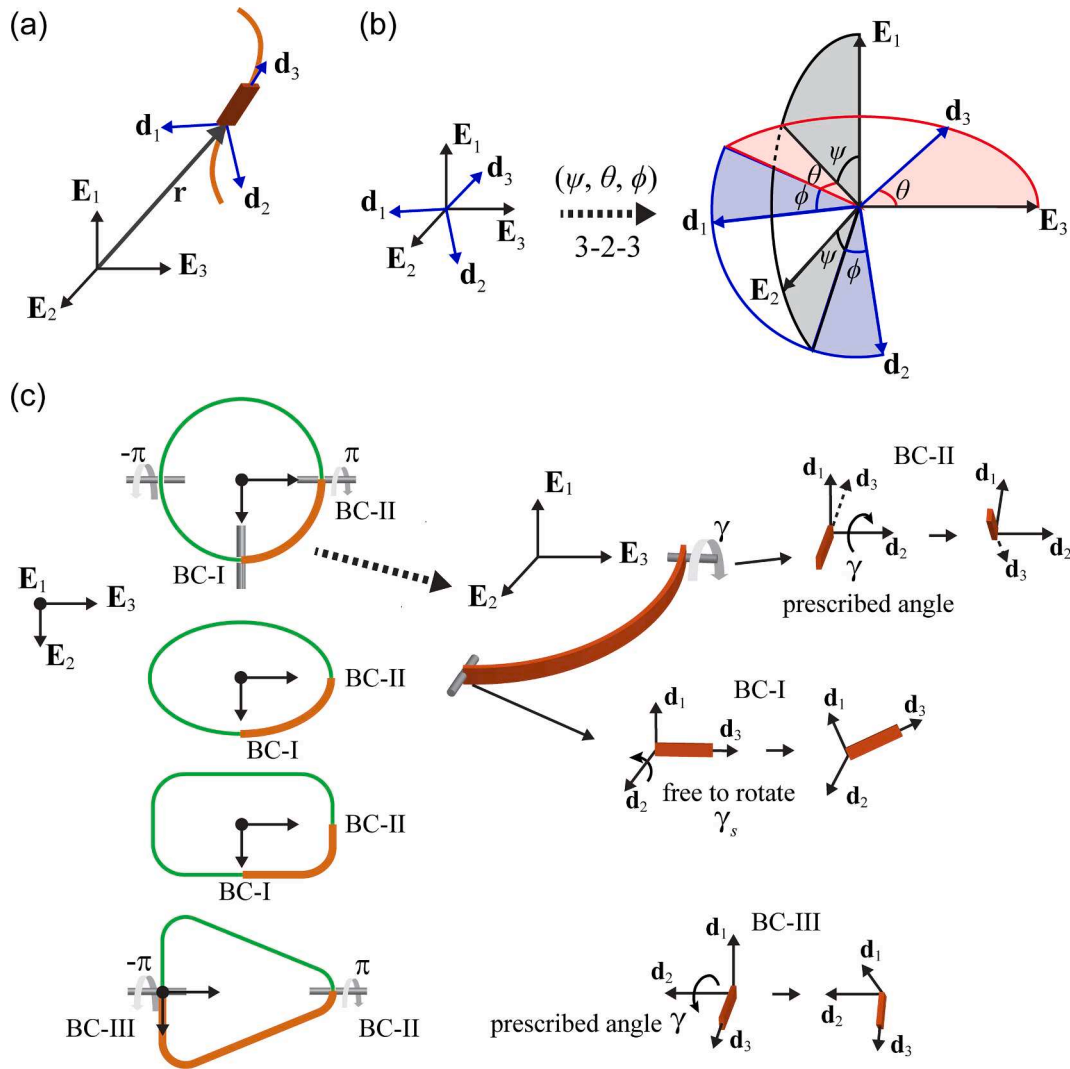
Fig. A1. Schematic of (a) the global and local director basis for a Kirchhoff rod, (b) the rotation defined using Euler angles with the 3–2-3 convention, and (c) the boundary conditions (BCs) for different ring geometries under the twisting loads.

where E is the Young's modulus and G the shear modulus of the material, which are related through $E = 2G(1 + \nu)$, with ν being the Poisson's ratio. The I_1, I_2 and J are the second moments and the torsion constant of the cross-section, respectively. For a rectangular cross-section with height h (in $\mathbf{d}_1$ direction) and thickness t (in $\mathbf{d}_2$ direction), they are given by (Timoshenko and Goodier, 1951)

$$I_1 = \frac{1}{12}ht^3, \ I_2 = \frac{1}{12}h^3t, \ J = \frac{ht^3}{3}\left[1 - \frac{192}{\pi^5}\frac{t}{h}\sum_{n=1}^{\infty}\frac{1}{(2n-1)^5}\tanh\left(\frac{\pi(2n-1)h}{2t}\right)\right] \tag{A8}$$

All the rings studied here stay naturally in a plane when unstressed, i.e., $k_2^{(u)} = k_3^{(u)} = 0$. In addition, the extensive and shear fdeformations are kinematically prescribed as zero (there is no constitutive relation for **F**). Inserting components of Eq. (A.7) into Eq. (A.6) leads to three modified equations as follows where k_i have replaced M_i to become the dependent variables.

$$k_1' = k_1^{(u)'} + \frac{1}{EI_1}F_2 + \left(\frac{I_2}{I_1} - \frac{GJ}{EI_1}\right)k_2k_3$$

$$k_2' = -\frac{1}{EI_2}F_1 - \left(\frac{I_1}{I_2} - \frac{GJ}{EI_2}\right)k_1k_3 + \frac{I_1}{I_2}k_1^{(u)}k_3 \tag{A9}$$

$$k_3' = \frac{EI_1 - EI_2}{GJ}k_1k_2 - \frac{EI_1}{GJ}k_1^{(u)}k_2$$

Next, the equilibrium Eqs. (A.5) and (A.9) are supplemented with the kinematic relations Eqs. (A.1) and (A.3) For easier specification of boundary conditions, we write $\mathbf{r}(s)$ in a global form as $\mathbf{r} = r_1\mathbf{E}_1 + r_2\mathbf{E}_2 + r_3\mathbf{E}_3$, where $(\mathbf{E}_1, \mathbf{E}_2, \mathbf{E}_3)$ is a global orthonormal basis, which is related to the local basis $(\mathbf{d}_1, \mathbf{d}_2, \mathbf{d}_3)$, with the help of quaternion parameterization of rotations, through (Healey and Mehta, 2005; Yu and Hanna, 2019)

$$\begin{Bmatrix} \mathbf{d}_1 \\ \mathbf{d}_2 \\ \mathbf{d}_3 \end{Bmatrix} = 2 \begin{pmatrix} q_0^2 + q_1^2 - \dfrac{1}{2} & q_1 q_2 + q_0 q_3 & q_1 q_3 - q_0 q_2 \\[2mm] q_1 q_2 - q_0 q_3 & q_0^2 + q_2^2 - \dfrac{1}{2} & q_2 q_3 + q_0 q_1 \\[2mm] q_1 q_3 + q_0 q_2 & q_2 q_3 - q_0 q_1 & q_0^2 + q_3^2 - \dfrac{1}{2} \end{pmatrix} \begin{Bmatrix} \mathbf{E}_1 \\ \mathbf{E}_2 \\ \mathbf{E}_3 \end{Bmatrix} = [\mathbf{Q}] \begin{Bmatrix} \mathbf{E}_1 \\ \mathbf{E}_2 \\ \mathbf{E}_3 \end{Bmatrix} \tag{A10}$$

where (q_0, q_1, q_2, q_3) are functions of arc length s and form a unit quaternion $\mathbf{q}$ whose inner product $|q| = q_0^2 + q_1^2 + q_2^2 + q_3^2 = 1$.

Assisted by Eqs. (A.10), Eq. (A.1) can be written in components

$$r_1^{'} = 2(q_1 q_3 + q_0 q_2), r_2^{'} = 2(q_2 q_3 - q_0 q_1), r_3^{'} = 2\left(q_0^2 + q_3^2 - \frac{1}{2} \right) \tag{A11}$$

which describes the kinematics for the rod centerline's position.

Taking derivative of Eq. (A.10) and substituting with Eq. (A.3), we obtain

$$[\mathbf{K}][\mathbf{Q}] = \frac{d}{ds}[\mathbf{Q}] \tag{A12}$$

Comparing components on two sides of Eq. (A.12) yields alternative equations for Eq. (A.3),

$$q_0^{'} = \frac{1}{2}(-q_1 k_1 - q_2 k_2 - q_3 k_3), q_1^{'} = \frac{1}{2}(q_0 k_1 - q_3 k_2 + q_2 k_3),$$
$$q_2^{'} = \frac{1}{2}(q_3 k_1 + q_0 k_2 - q_1 k_3), q_3^{'} = \frac{1}{2}(-q_2 k_1 + q_1 k_2 + q_0 k_3). \tag{A13}$$

which describes the kinematics for the rod cross-section's orientations.

Combining Eqs. (A.5), (A.9), (A.11) and (A.13) gives a system of thirteen equations. We perform the normalization on relevant variables and derivative-operator through

$$(\bar{r}_i, \bar{s}) = \frac{(r_i, s)}{L}, \quad \left(\bar{k}_i, \bar{k}_i^{(u)} \right) = \left(k_i, k_i^{(u)} \right) L, \quad \bar{F}_i = \frac{L^2}{GJ} F_i, \quad (\cdot)^{'} = \frac{d(\cdot)}{d\bar{s}} \frac{1}{L} \tag{A14}$$

where L is a reference length and will vary for different ring geometries. Thus the dimensionless arc length $\bar{s} \in [0, L_0/L]$. Dropping the bars (i.e., using original symbols to represent the normalized variables) for convenience, one obtains the dimensionless governing equations,

$$F_1^{'} = F_2 k_3 - F_3 k_2, \ F_2^{'} = F_3 k_1 - F_1 k_3, \ F_3^{'} = F_1 k_2 - F_2 k_1$$
$$k_1^{'} = k_1^{(u)'} + \frac{1}{\alpha} F_2 + \left(\frac{\beta}{\alpha} - \frac{1}{\alpha} \right) k_2 k_3$$
$$k_2^{'} = -\frac{1}{\beta} F_1 - \left(\frac{\alpha}{\beta} - \frac{1}{\beta} \right) k_1 k_3 + \frac{\alpha}{\beta} k_1^{(u)} k_3$$
$$k_3^{'} = (\alpha - \beta) k_1 k_2 - \alpha k_1^{(u)} k_2 \tag{A15}$$
$$q_0^{'} = \frac{1}{2}(-q_1 k_1 - q_2 k_2 - q_3 k_3), q_1^{'} = \frac{1}{2}(q_0 k_1 - q_3 k_2 + q_2 k_3)$$
$$q_2^{'} = \frac{1}{2}(q_3 k_1 + q_0 k_2 - q_1 k_3), q_3^{'} = \frac{1}{2}(-q_2 k_1 + q_1 k_2 + q_0 k_3)$$
$$r_1^{'} = 2(q_1 q_3 + q_0 q_2), r_2^{'} = 2(q_2 q_3 - q_0 q_1), r_3^{'} = 2\left(q_0^2 + q_3^2 - \frac{1}{2} \right)$$

where here and in the main text $(\cdot)^{'} = d(\cdot)/d\bar{s}$ and all symbols represent dimensionless quantities unless otherwise specified, α and β are dimensionless bending-to-torsional rigidity ratios of the cross-section, which are given by

$$\alpha = \frac{EI_1}{GJ} = \frac{(1+\nu)}{2\lambda} \text{ and } \beta = \frac{EI_2}{GJ} = \frac{(1+\nu)}{2\lambda}\left(\frac{h}{t} \right)^2 \text{ with}$$
$$\lambda\left(\frac{h}{t} \right) = \left[1 - \frac{192}{\pi^5} \frac{t}{h} \sum_{n=1}^{\infty} \frac{1}{(2n-1)^5} \tanh\left(\frac{\pi(2n-1)}{2} \frac{h}{t} \right) \right] \tag{A16}$$

A.2. Boundary conditions

We consider the circular rings and give the boundary conditions for the twisting loads. The 1/4 model is considered here due to the anti-symmetry at quarter points (Yoshiaki et al., 1992). Let the reference length L be the radius of the circular ring, denoted as R, thus the natural curvature $k_1^{(u)}$ is 1 and the arc length s is in $[0, \pi/2]$. The Euler angles are used to define the rotational boundary conditions (see Fig. A.1b-A.1c, Appendix A.3), which are then converted into those in terms of the quaternion components (q_0, q_1, q_2, q_3) using Eq. (A.24) (Appendix A.3).

First, we consider the $s = 0$ boundary (BC-I of Fig. A.1c). For rotational degree-of-freedoms (DOFs), the rod end remains perpendicular to the initial $\mathbf{d}_2$

axis and is free to rotate around $\mathbf{d}_2$. Let γ_s be the unknown rotation angle, and then the Euler angles can be obtained as $\psi = 0, \theta = \gamma_s, \phi = 0$, which leads to $q_0 = \cos\frac{\gamma_s}{2}, q_1 = 0, q_2 = \sin\frac{\gamma_s}{2}, q_3 = 0$. The angle γ_s is not prescribed, implying $M_2 = 0$. Therefore, we have

$$q_1(0) = 0, \quad q_3(0) = 0, \quad k_2(0) = 0 \tag{A17}$$

For translational DOFs, the rod end is free to translate on the initial $\mathbf{d}_2$ axis (same direction with $\mathbf{E}_2$ axis) with arbitrary r_2 position, so we have

$$r_1(0) = 0, \quad r_3(0) = 0, \quad F_2(0) = 0 \tag{A18}$$

Second, we consider the $s = \pi/2$ boundary (BC-II of Fig. A.1c). Since the local basis has different orientations from the global basis, we recall that the components for position $\mathbf{r}$ are defined in the global basis, while those for $\mathbf{M}$ (or $\mathbf{k}$) and $\mathbf{F}$ are in the local basis. For translational DOFs, the end is free to translate on the initial $\mathbf{d}_2$ axis (same direction with $\mathbf{E}_3$ axis) with arbitrary r_3 position, so we have

$$r_1\left(\frac{\pi}{2}\right) = 0, \quad F_2\left(\frac{\pi}{2}\right) = 0, \quad r_2\left(\frac{\pi}{2}\right) = 0 \tag{A19}$$

For the rotational DOFs, we obtain the Euler angles as $\psi = -\frac{1}{2}\pi - \gamma, \theta = \frac{1}{2}\pi, \phi = \frac{1}{2}\pi$, where γ is the prescribed twisting angle. Using Eq. (A.24) (Appendix A.3), we obtain

$$q_0\left(\frac{\pi}{2}\right) = \frac{\sqrt{2}}{2}\cos\frac{\gamma}{2}, \quad q_1\left(\frac{\pi}{2}\right) = \frac{\sqrt{2}}{2}\cos\frac{\gamma}{2}, \quad q_2\left(\frac{\pi}{2}\right) = -\frac{\sqrt{2}}{2}\sin\frac{\gamma}{2}, \quad q_3\left(\frac{\pi}{2}\right) = -\frac{\sqrt{2}}{2}\sin\frac{\gamma}{2} \tag{A20}$$

Eqs. (A.17)-(A.20) provide thirteen boundary conditions, which are sufficient for thirteen unknowns. There is one additional boundary condition $q_0(0)^2 + q_2(0)^2 = 1$ at the $s = 0$ boundary, which is implied already and does not need to be specified since (1) Eq. (A.15)$_{7\text{-}10}$ for q_i implies that $|\mathbf{q}|$ is a constant, which must equal to 1 once the $q_i(\pi/2)$ that meet $|\mathbf{q}| = 1$ are specified; and (2) $q_1(0) = q_2(0) = 0$. As a result, the BVP system is well-posed for the single-segment ring folding problem.

Once the system is solved, using the corresponding curvature component (i.e., k_2) and the constitutive law Eq. (A.7), the external moment (denoted by M) that is required to prescribe the angle γ can be obtained as

$$\overline{M} = ML/GJ = M_2L/GJ = \beta\bar{k}_2 \tag{A21}$$

Here, bars are included to represent dimensionless quantities.

A.3. Relation between Euler angle and quaternion description of rotations

Rotation of the local director basis ($\mathbf{d}_1, \mathbf{d}_2, \mathbf{d}_3$) is parameterized using the quaternion number, which is singularity-free. For any rotations in 3D space, there exists an axis $\mathbf{a}$ around which the rotation angle is ω. Then (q_0, q_1, q_2, q_3), called Euler parameters, can be introduced (Healey and Mehta, 2005):

$$q_0 = \cos\left(\frac{\omega}{2}\right), \quad (q_1, q_2, q_3) = \mathbf{a}\sin\left(\frac{\omega}{2}\right) \tag{A22}$$

A unit quaternion $\mathbf{q} = (q_0, q_1, q_2, q_3)$ can then be defined, which satisfies $|\mathbf{q}| = q_0^2 + q_1^2 + q_2^2 + q_3^2 = 1$. With such definition, a rotation matrix can be written in terms of quaternion components, as given in Eq. (10), which relates the rotated local basis ($\mathbf{d}_1, \mathbf{d}_2, \mathbf{d}_3$) and the global basis ($\mathbf{E}_1, \mathbf{E}_2, \mathbf{E}_3$) (see Fig. A.1b). Alternatively, using Euler angles (ψ, θ, ϕ) and following the 3–2-3 rotation convention(Love, 2013; Healey and Mehta, 2005; Yu and Hanna, 2019) (see Fig. A.1b), i.e., the local basis rotates around $\mathbf{d}_3$ by ψ, then around rotated $\mathbf{d}_2$ by θ and finally around rotated $\mathbf{d}_3$ by ϕ, the relation between the local basis and global basis can be written as

$$\begin{Bmatrix} \mathbf{d}_1 \\ \mathbf{d}_2 \\ \mathbf{d}_3 \end{Bmatrix} = \begin{pmatrix} \cos\phi & \sin\phi & 0 \\ -\sin\phi & \cos\phi & 0 \\ 0 & 0 & 1 \end{pmatrix} \begin{pmatrix} \cos\theta & 1 & -\sin\theta \\ 1 & 1 & 0 \\ \sin\theta & 0 & \cos\theta \end{pmatrix} \begin{pmatrix} \cos\psi & \sin\psi & 0 \\ -\sin\psi & \cos\psi & 0 \\ 0 & 0 & 1 \end{pmatrix} \begin{Bmatrix} \mathbf{E}_1 \\ \mathbf{E}_2 \\ \mathbf{E}_3 \end{Bmatrix} \tag{A23}$$

Comparing Eqs. (A.10) and (A.23) leads to relations between quaternion components and Euler angles as follows,

$$q_0 = \cos\frac{\theta}{2}\cos\frac{\phi + \psi}{2}, q_1 = \sin\frac{\theta}{2}\sin\frac{\phi - \psi}{2}, q_2 = \sin\frac{\theta}{2}\cos\frac{\phi - \psi}{2}, q_3 = \cos\frac{\theta}{2}\sin\frac{\phi + \psi}{2} \tag{A24}$$

Eq. (A.24) will help us to specify the boundary conditions for ring folding problem.

To obtain the boundary conditions for the quaternion components (q_0, q_1, q_2, q_3), we first specify the rotational boundary conditions in terms of Euler angles using geometric conditions (Fig. A.1b) for certain loads, which are then substituted into to give the final forms. The boundary conditions for the twisting of differently shaped rings are schematically illustrated in Fig. A.1c.

Appendix B. Folded shape and areal packing ratio by planar rod models

We use a reduced planar rod model to evaluate the folded shapes of differently shaped rings, which are assumed to be three-looped, implying an angle change 6π over the entire ring. The curvature k_1 is the sum of the natural curvature $k_1^{(u)}$ and the curvature k_d due to deformation. The geometric condition requires $\int_0^{L_0} k_1^{(u)} ds = 2\pi$ and $\int_0^{L_0} k_1 ds = 6\pi$, which leads to $\int_0^{L_0} k_d ds = 4\pi$. Since the folded ring is in a planar configuration, it should have in-plane curvatures only without producing any out-of-plane moments, i.e., $\mathbf{M} = (M_1, 0, 0)$ in the frame ($\mathbf{d}_1, \mathbf{d}_2, \mathbf{d}_3$) with $M_1 = EI_1k_d$ and $k_d (\equiv k_1 - k_1^{(u)})$. In turn, the vanishing twisting moment M_2 (Eq. (A.21)) at $\gamma = \pi$ implies that the ring is folded into a planar (three-covered) shape. The $M_2(\gamma = \pi) = 0$ is thus used as a criterion for determining the foldability.

We consider the rings with two symmetric axes (excluding triangular rings). In this case, the internal force $\mathbf{F} = (0, 0, 0)$ can be assumed, which upon using Eqs. (6) and (7) implies constant M_1 and k_d along the ring. Therefore, k_d can be written as

$$k_d = 4\pi/L_0 \tag{B1}$$

The entire length L_0 depends on the specific ring shape. With the k_1 given in Eq. (B.1) and the in-plane condition, which, in our case, implies $q_0 = q_1$

$= 0$ and $r_1 = 0$, the Eq. (14)$_{7\text{-}13}$ reduces to

$$q_2' = \frac{1}{2}q_3 k_1, \ q_3' = -\frac{1}{2}q_2 k_1,$$
$$r_2' = 2q_2 q_3, \ r_3' = 2q_3^2 - 1 \tag{B2}$$

The constraint $q_2^2 + q_3^2 = 1$ is implied. The symmetry allows us to consider the 1/4 model. At the starting end ($s = 0$), the variables in Eq. (B.2) can be specified as

$$q_2(0) = 1, \ q_3(0) = 0$$
$$r_2(0) = 0, \ r_3(0) = 0 \tag{B3}$$

Eqs. (B.2) and (B.3) form an initial value problem (IVP).

For elliptical rings, the ODE system should be re-parameterized with respect to τ following the method described in Section 2.1.2, such that $k_1 = k_1^{(u)} + k_d$ can be analytically expressed, where $k_1^{(u)}$ is given in Eq. (21) and k_d can be obtained using Eq. (B.1) as

$$k_d = \frac{4\pi}{\int_0^{2\pi} \sqrt{(b\sin\tau)^2 + (a\cos\tau)^2}\,d\tau} = \frac{\pi}{aE\left(1 - \left(\frac{b}{a}\right)^2\right)} \tag{B4}$$

where $E(p)$ denotes the complete elliptic integral of the second kind with $0 < p < 1$. The re-formulated system can be solved using MATLAB through routine ode45 to give the folded ring shapes. The envelope area of the folded shape can then be calculated and used to evaluate the areal packing ratio.

For rounded rectangular rings, the ODE system can be analytically solved. The 1/4 geometry consists of three segments that have distinct natural curvatures, which are given as

$$\bar{k}_1^{(u)} = k_1^{(u)}r = \begin{cases} 0, & 0 < \bar{s} < c_1 \\ 1, & c_1 < \bar{s} < c_1 + \pi/2 \\ 0, & c_1 + \pi/2 < \bar{s} < c_1 + c_2 + \pi/2 \end{cases} \tag{B5}$$

where the fillet radius r has been used as the reference length L for normalization (see Eq. (13)), $c_1 (\equiv a/r - 1)$, $\pi/2$ and $c_2 (\equiv b/r - 1)$ are dimensionless segment lengths, a and b are the lengths of the semi-horizontal axis ($\mathbf{E}_3$-axis, see Fig. A.1c) and semi-vertical axis ($\mathbf{E}_2$-axis), respectively. By using Eq. (B.1) we can write the dimensionless curvature due to deformation as

$$\bar{k}_d = \frac{\pi}{c_1 + \frac{1}{2}\pi + c_2} \tag{B6}$$

Then, the curvature $k_1 \equiv k_1^{(u)} + k_d$ for each segment is obtained. We observe that k_1 is constant for each segment, thus Eq.$_{1\text{-}2}$ implies $4q_2'' + k_1^2 q_2 = 0$ and admits the general solution $q_2 = \cos\left(\frac{k_1 x - \Theta}{2}\right)$ and $q_3 = -\sin\left(\frac{k_1 x - \Theta}{2}\right)$ where Θ is constant for each segment. Applying Eq.$_{1\text{-}2}$ and continuous conditions of q_2 and q_3 at segment joints gives q_2 and q_3 as

$q_2 = \cos(\varphi(\bar{s}))$ and $q_3 = -\sin(\varphi(\bar{s}))$, with

$$\varphi(x) = \begin{cases} \frac{1}{2}\bar{k}_d\bar{s}, & 0 < \bar{s} < c_1 \\[2mm] \frac{1}{2}(\bar{k}_d + 1)\bar{s} - \frac{1}{2}c_1, & c_1 < \bar{s} < c_1 + \pi/2 \\[2mm] \frac{1}{2}\bar{k}_d\bar{s} + \frac{\pi}{4}, & c_1 + \pi/2 < \bar{s} < c_1 + c_2 + \pi/2 \end{cases} \tag{B7}$$

Substituting q_2 and q_3 into Eq.$_{3\text{-}4}$ and integrating from 0 to $c_1 + c_2 + \pi/2$ gives forms of r_2 and r_3 of the folded ring,

$$\bar{r}_2 = \begin{cases} \frac{1}{\bar{k}_d}\cos(\bar{k}_d\bar{s}) + \frac{1}{\bar{k}_d(\bar{k}_d + 1)}\left[\cos\left(\bar{k}_d\left(c_1 + \frac{\pi}{2}\right) + \frac{\pi}{2}\right) - \cos(\bar{k}_d c_1)\right], & 0 < \bar{s} < c_1 \\[3mm] \frac{1}{\bar{k}_d + 1}\cos(\bar{k}_d\bar{s} + \bar{s} - c_1) + \frac{1}{\bar{k}_d(\bar{k}_d + 1)}\cos\left(\bar{k}_d\left(c_1 + \frac{\pi}{2}\right) + \frac{\pi}{2}\right), & c_1 < \bar{s} < c_1 + \pi/2 \\[3mm] \frac{1}{\bar{k}_d}\cos\left(\bar{k}_d\bar{s} + \frac{\pi}{2}\right), & c_1 + \pi/2 < \bar{s} < c_1 + c_2 + \pi/2 \end{cases} \tag{B8}$$

$$\bar{r}_3 = \begin{cases} -\frac{1}{\bar{k}_d}\sin(\bar{k}_d\bar{s}), & 0 < \bar{s} < c_1 \\[3mm] -\frac{1}{\bar{k}_d + 1}\sin(\bar{k}_d\bar{s} + \bar{s} - c_1) - \frac{1}{\bar{k}_d(\bar{k}_d + 1)}\sin(\bar{k}_d c_1), & c_1 < \bar{s} < c_1 + \pi/2 \\[3mm] -\frac{1}{\bar{k}_d}\sin\left(\bar{k}_d\bar{s} + \frac{\pi}{2}\right) + \frac{1}{\bar{k}_d(\bar{k}_d + 1)}\left[\sin\left(\bar{k}_d\left(c_1 + \frac{\pi}{2}\right) + \frac{\pi}{2}\right) - \sin(\bar{k}_d c_1)\right], \\[2mm] \quad\quad c_1 + \pi/2 < \bar{s} < c_1 + c_2 + \pi/2 \end{cases}$$

Here, $r_2(s)$ has been subtracted by a constant such that $r_2(c_1 + c_2 + \pi/2) = 0$ is consistent with the boundary conditions presented in Appendix A.2. The envelope area of the folded shape is calculated and used to evaluate the areal packing ratio.

Appendix C. More results on circular rings

C.1. Further continuation on the h/t = 1 case

Fig. C.1 shows the normalized twisting moment Ma/GJ versus angle γ curve, as well as the snapshots (from I to VIII) of deformed shapes at different γ values, for the circular ring with $h/t = 1$ obtained using rod theory. We see that when γ is allowed to exceed π, the continuation results in a complex equilibrium path, which can eventually arrive at the equilibrium solution for the folded three-covered shape at $\gamma = \pi$ (see the state VIII). However, this solution is neither accessible nor stable under the simple twisting with γ varying from 0 to π. Therefore, the $h/t = 1$ case is identified as an un-foldable case and so do the similar cases throughout the paper.
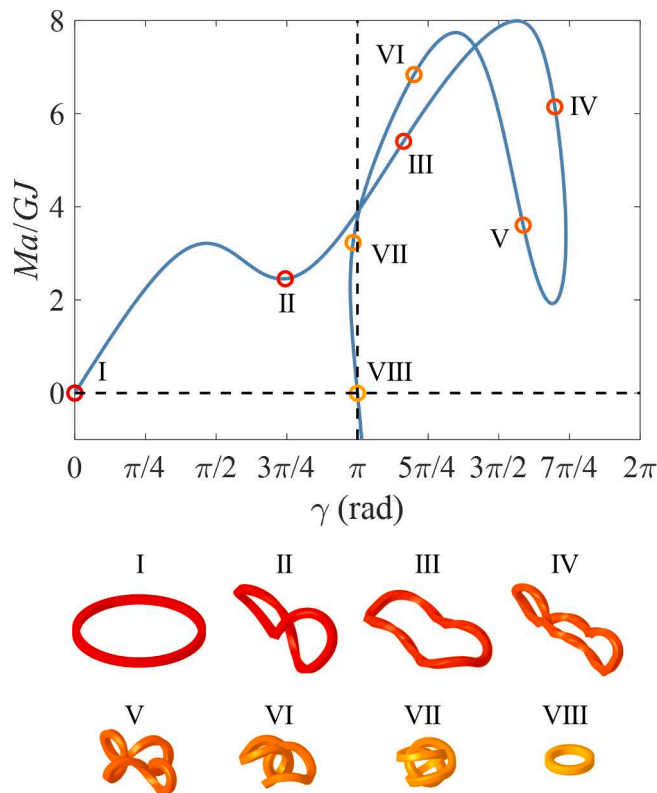

Fig. C1. Folding of the circular ring with $h/t = 1.0$. The MR/GJ versus γ curve is obtained by numerical continuation on γ which can exceed π. Snapshots of deformed shapes at different γ values are provided.

C.2. Strain energy-angle plots of representative cases
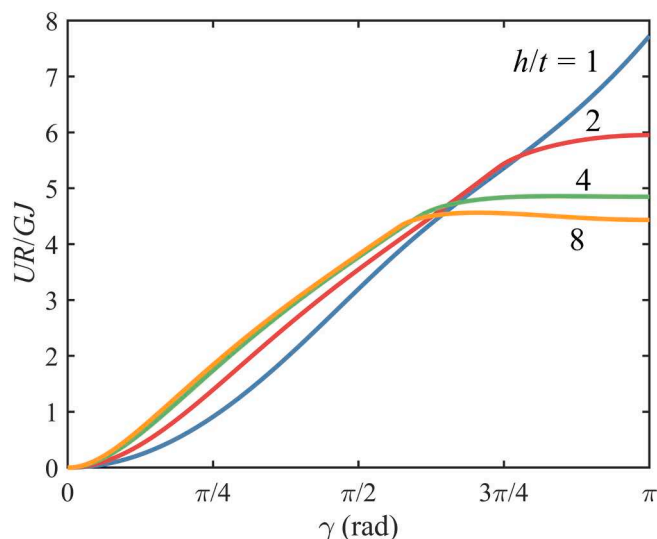

Fig. C2. Normalized strain energy UR/GJ versus γ curves for circular rings with different h/t values.

Appendix D. More comparisons between the rod model and FEA

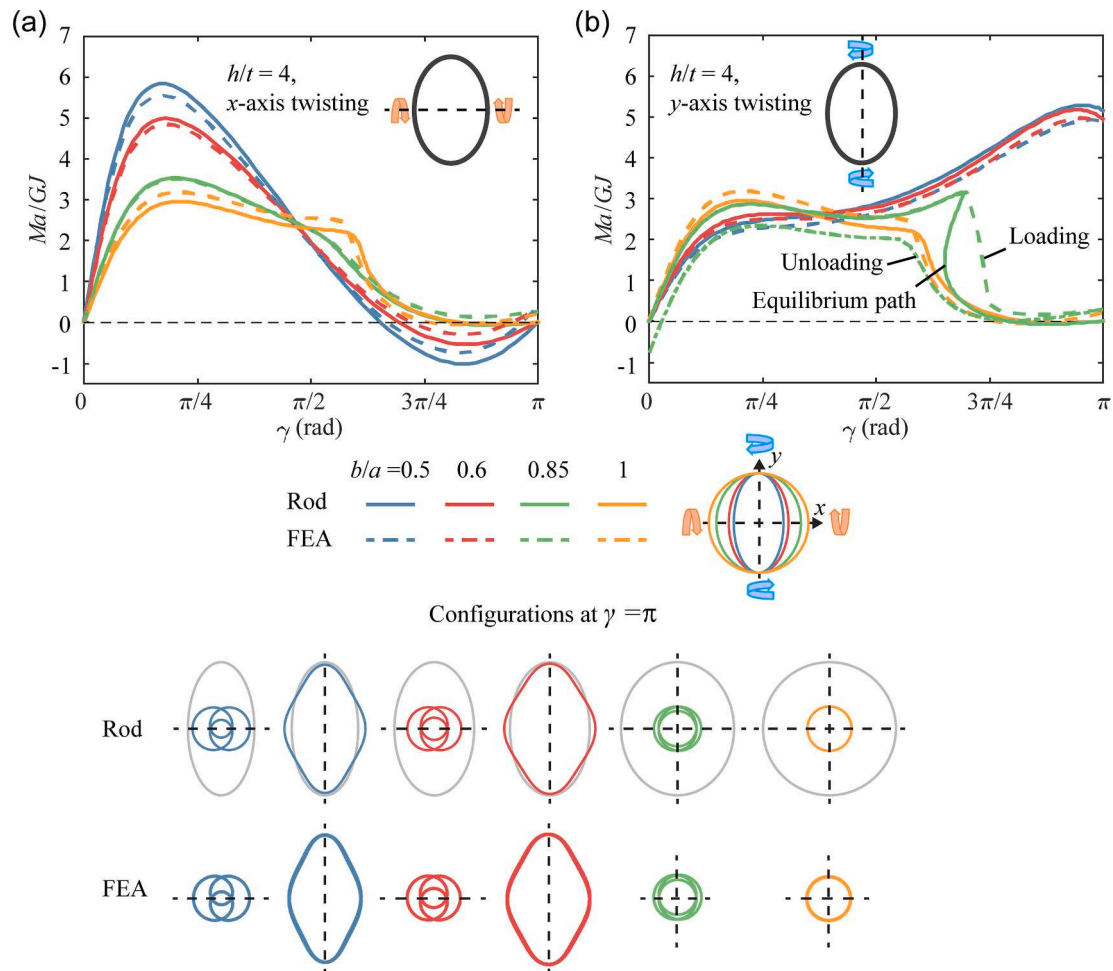### D.1. Elliptical rings

Fig. D1. Elliptical ring folding through twisting. The Ma/GJ versus γ curves obtained using the rod model and FEA for fixed $h/t = 4.0$ and different b/a values and twisting axes: (a) x-axis, (b) y-axis. In (b), snap-back instability appears for $b/a = 0.85$. Hysteresis in FEA loading–unloading curves verifies such behavior. The initial ($\gamma = 0$, light gray) and final ($\gamma = \pi$, colored) configurations for these cases are provided at the bottom. The twisting axes are indicated by the black dashed lines.
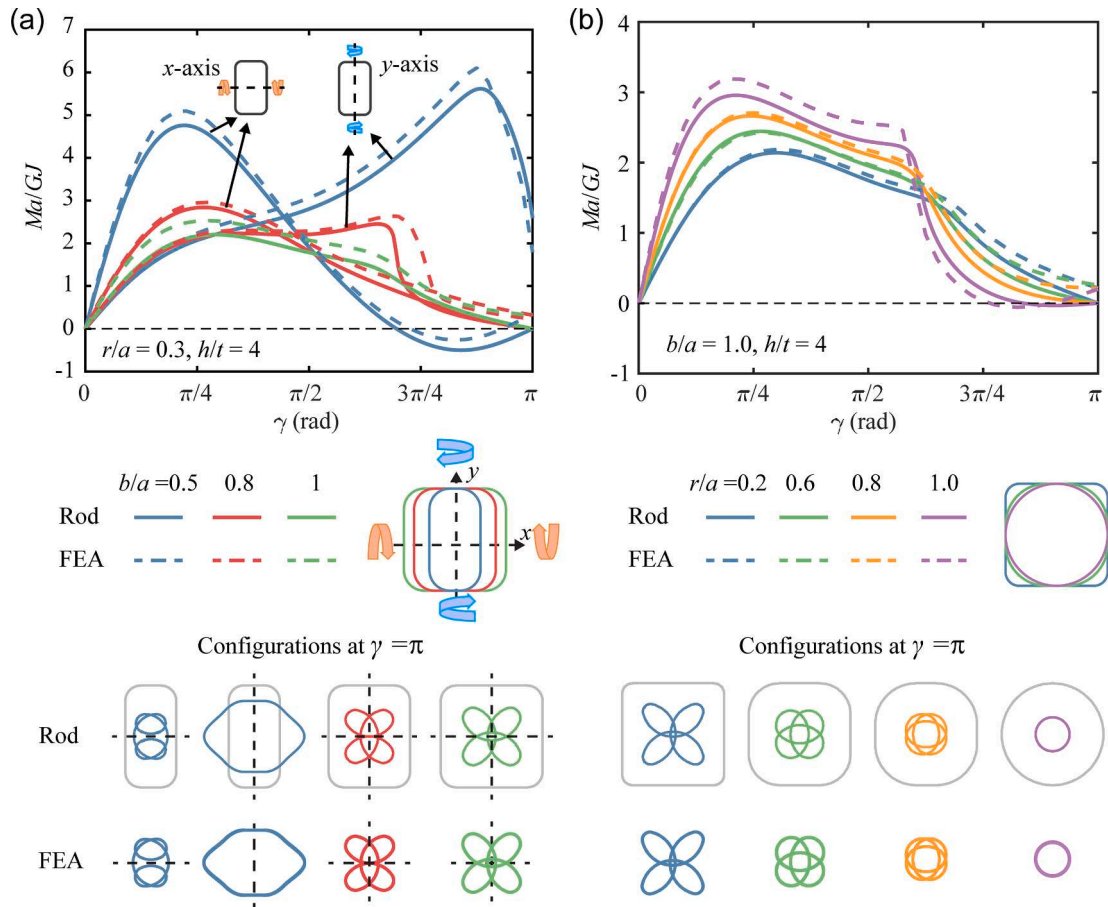
D.2. Rounded rectangular rings

Fig. D2. Folding of rounded rectangular rings through twisting. The Ma/GJ versus γ curves obtained using the rod model and FEA for different cases. (a) $r/a = 0.3$, $h/t = 4.0$ and different b/a values. (b) $b/a = 1.0$, $h/t = 4.0$ and different r/a values. The initial ($\gamma = 0$, light gray) and final ($\gamma = \pi$, colored) configurations for these cases are provided at the bottom. The black dashed lines indicate the twisting axes. The folded shape is sensitive to not only the profile b/a but also the fillet size r/a, although the original shape seems to be insensitive to r/a.
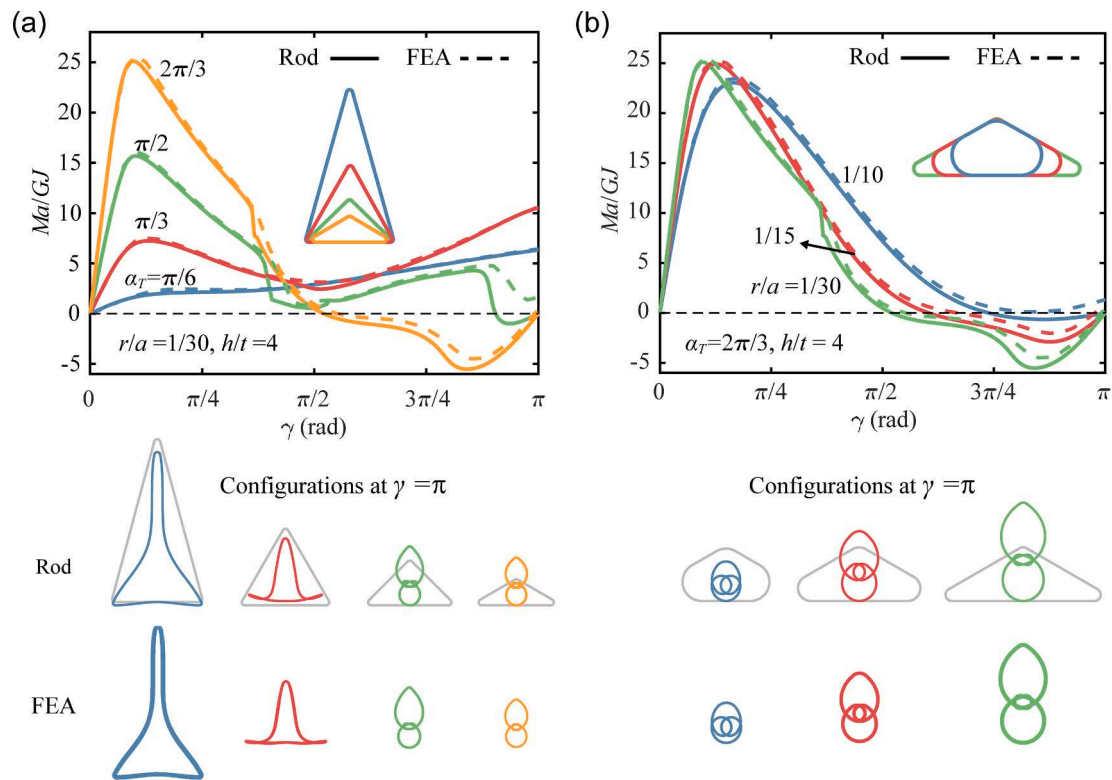
D.3. Rounded triangular rings

Fig. D3. Folding of rounded triangular rings through twisting. The Ma/GJ versus γ curves obtained using the rod model and FEA for different cases. (a) $r/a = 1/30$, $h/t = 4.0$ and different α_T values. (b) $\alpha_T = 2\pi/3$, $h/t = 4.0$ and different r/a values. The initial ($\gamma = 0$, light gray) and final ($\gamma = \pi$, colored) configurations for these cases are provided at the bottom.

References

Zirbel, S.A., Lang, R.J., Thomson, M.W., Sigel, D.A., Walkemeyer, P.E., Trease, B.P., Magleby, S.P., Howell, L.L., 2013. Accommodating thickness in origami-based deployable arrays1. J. Mech. Design 135 (11).

Melancon, D., Gorissen, B., García-Mora, C.J., Hoberman, C., Bertoldi, K., 2021. Multistable inflatable origami structures at the metre scale. Nature 592 (7855), 545–550.

Dudte, L.H., Vouga, E., Tachi, T., Mahadevan, L., 2016. Programming curvature using origami tessellations. Nat. Mater. 15 (5), 583–588.

Callens, S.J.P., Zadpoor, A.A., 2018. From flat sheets to curved geometries: origami and kirigami approaches. Mater. Today 21 (3), 241–264.

Martinez, R.V., Fish, C.R., Chen, X., Whitesides, G.M., 2012. Elastomeric origami: programmable paper-elastomer composites as pneumatic actuators. Adv. Funct. Mater. 22 (7), 1376–1384.

Li, S., Vogt, D.M., Rus, D., Wood, R.J., 2017. Fluid-driven origami-inspired artificial muscles. Proc. Natl. Acad. Sci. 114 (50), 13132–13137.

Wu, S., Ze, Q., Dai, J., Udipi, N., Paulino, G.H., Zhao, R., 2021. Stretchable origami robotic arm with omnidirectional bending and twisting. Proc. Natl. Acad. Sci. 118 (36), e2110023118.

Silverberg, J.L., Evans, A.A., McLeod, L., Hayward, R.C., Hull, T., Santangelo, C.D., Cohen, I., 2014. Using origami design principles to fold reprogrammable mechanical metamaterials. Science 345 (6197), 647–650.

Filipov, E.T., Tachi, T., Paulino, G.H., 2015. Origami tubes assembled into stiff, yet reconfigurable structures and metamaterials. Proc. Natl. Acad. Sci. 112 (40), 12321–12326.

Zhai, Z., Wang, Y., Jiang, H., 2018. Origami-inspired, on-demand deployable and collapsible mechanical metamaterials with tunable stiffness. Proc. Natl. Acad. Sci. 115 (9), 2032–2037.

Nauroze, S.A., Novelino, L.S., Tentzeris, M.M., Paulino, G.H., 2018. Continuous-range tunable multilayer frequency-selective surfaces using origami and inkjet printing. Proc. Natl. Acad. Sci. 115 (52), 13210–13215.

Novelino, L.S., Ze, Q., Wu, S., Paulino, G.H., Zhao, R., 2020. Untethered control of functional origami microrobots with distributed actuation. Proc. Natl. Acad. Sci. 117 (39), 24096–24101.

Shim, J., Perdigou, C., Chen, E.R., Bertoldi, K., Reis, P.M., 2012. Buckling-induced encapsulation of structured elastic shells under pressure. Proc. Natl. Acad. Sci. 109 (16), 5978–5983.

Nasto, A., Ajdari, A., Lazarus, A., Vaziri, A., Reis, P.M., 2013. Localization of deformation in thin shells under indentation. Soft Matter 9 (29), 6796–6803.

Stein-Montalvo, L., Costa, P., Pezzulla, M., Holmes, D.P., 2019. Buckling of geometrically confined shells. Soft Matter 15 (6), 1215–1222.

Bende, N.P., Evans, A.A., Innes-Gold, S., Marin, L.A., Cohen, I., Hayward, R.C., Santangelo, C.D., 2015. Geometrically controlled snapping transitions in shells with curved creases. Proc. Natl. Acad. Sci. 112 (36), 11175–11180.

Liu, Y., Yan, Z., Lin, Q., Guo, X., Han, M., Nan, K., Hwang, K.-C., Huang, Y., Zhang, Y., Rogers, J.A., 2016. Guided formation of 3D helical mesostructures by mechanical buckling: analytical modeling and experimental validation. Adv. Funct. Mater. 26 (17), 2909–2918.

Shan, S., Kang, S.H., Raney, J.R., Wang, P., Fang, L., Candido, F., Lewis, J.A., Bertoldi, K., 2015. Multistable architected materials for trapping elastic strain energy. Adv. Mater. 27 (29), 4296–4301.

Yoshiaki, G., Yasuhito, W., Toshihiro, K., Makoto, O., 1992. Elastic buckling phenomenon applicable to deployable rings. Int. J. Solids Struct. 29 (7), 893–909.

Audoly, B., Seffen, K.A., 2015. Buckling of naturally curved elastic strips: the ribbon model makes a difference. J. Elast. 119 (1), 293–320.

Bae, J., Na, J.-H., Santangelo, C.D., Hayward, R.C., 2014. Edge-defined metric buckling of temperature-responsive hydrogel ribbons and rings. Polymer 55 (23), 5908–5914.

Mouthuy, P.-O., Coulombier, M., Pardoen, T., Raskin, J.-P., Jonas, A.M., 2012. Overcurvature describes the buckling and folding of rings from curved origami to foldable tents. Nat. Commun. 3 (1), 1290.

Mahadevan, L., Keller, J.B., 1993. The shape of a Möbius band. Proc. R. Soc. Lond. A 1908 (440), 149–162.

Manning, R.S., Hoffman, K.A., 2001. Stability of n-covered Circles for Elastic Rods with Constant Planar Intrinsic Curvature. J. Elasticity Phys. Sci. Solids 62 (1), 1–23.

Goriely, A., Tabor, M., 1997. Nonlinear dynamics of filaments I Dynamical instabilities. Phys. D Nonlinear Phenomena 105 (1), 20–44.

Moulton, D.E., Lessinnes, T., Goriely, A., 2013. Morphoelastic rods. Part I: a single growing elastic rod. J. Mech. Phys. Solids 61 (2), 398–427.

Dias, M.A., Audoly, B., 2014. A non-linear rod model for folded elastic strips. J. Mech. Phys. Solids 62, 57–80.

Dias, M.A., Santangelo, C.D., 2012. The shape and mechanics of curved-fold origami structures. EPL (Europhysics Letters) 100 (5), 54005.

Wu, S., Yue, L., Jin, Y., Sun, X., Zemelka, C., Qi, H.J., Zhao, R., 2021. Ring Origami: Snap-Folding of Rings with Different Geometries. Adv. Intell. Syst. 3 (9), 2100107.

Crisfield, M.A., 1981. A fast incremental/iterative solution procedure that handles "snap-through". Comput. Struct. 13 (1), 55–62.

Crisfield, M.A., 1986. Snap-through and snap-back response in concrete structures and the dangers of under-integration. Int. J. Numer. Meth. Eng. 22 (3), 751–767.

Love, A.E.H., 2013. A treatise on the mathematical theory of elasticity. Cambridge University Press.

O'Reilly, O.M., 2017. Modeling nonlinear problems in the mechanics of strings and rods. Springer.

Goriely, A., Tabor, M., 1998. Spontaneous helix hand reversal and tendril perversion in climbing plants. Phys. Rev. Lett. 80 (7), 1564–1567.

Fuller, F.B., 1978. Decomposition of the linking number of a closed ribbon: a problem from molecular biology. Proc. Natl. Acad. Sci. 75 (8), 3557–3561.

Healey, T.J., Mehta, P.G., 2005. Straightforward computation of spatial equilibria of geometrically exact cosserat rods. Int. J. Bifurcation Chaos 15 (03), 949–965.

Sano, T.G., Wada, H., 2019. Twist-Induced Snapping in a Bent Elastic Rod and Ribbon. Phys. Rev. Lett. 122 (11), 114301.

Yu, T., Hanna, J.A., 2019. Bifurcations of buckled, clamped anisotropic rods and thin bands under lateral end translations. J. Mech. Phys. Solids 122, 657–685.

McMillen, 2002. Tendril perversion in intrinsically curved rods. J. Nonlinear Sci. 12 (3), 241–281.

Haijun, Z., Zhong-can, O.-Y., 1998. Spontaneous curvature-induced dynamical instability of Kirchhoff filaments: application to DNA kink deformations. J. Chem. Phys. 110 (2), 1247–1251.

Huang, J., Liu, J., Kroll, B., Bertoldi, K., Clarke, D.R., 2012. Spontaneous and deterministic three-dimensional curling of pre-strained elastomeric bi-strips. Soft Matter 8 (23), 6291–6300.

Liu, J.; Huang, J.; Su, T.; Bertoldi, K.; Clarke, D. R., Structural Transition from Helices to Hemihelices. *PLOS ONE* **2014,** *9* (4), e93183.

Wang, D.; Thouless, M. D.; Lu, W.; Barber, J. R., Generation of perversions in fibers with intrinsic curvature. *J Mech Phys Solids* **2020,** *139*, 103932.

Goriely, A., Tabor, M., 2000. The nonlinear dynamics of filaments. Nonlinear Dyn. 21 (1), 101–133.

Goriely, A., Nizette, M., Tabor, M., 2001. On the dynamics of elastic strips. J. Nonlinear Sci. 11 (1), 3–45.

Lessinnes, T., Moulton, D.E., Goriely, A., 2017. Morphoelastic rods Part II: Growing birods. J. Mech. Phys. Solids 100, 147–196.

Moulton, D. E.; Lessinnes, T.; Goriely, A., Morphoelastic rods III: Differential growth and curvature generation in elastic filaments. *J Mech Phys Solids* **2020,** *142*, 104022.

Moore, A., Healey, T., 2019. Computation of elastic equilibria of complete Möbius bands and their stability. Mathemat. Mech. Solids 24 (4), 939–967.

Jawed, M.K., Dieleman, P., Audoly, B., Reis, P.M., 2015. Untangling the mechanics and topology in the frictional response of long overhand elastic knots. Phys. Rev. Lett. 115 (11), 118302.

Patil, V.P., Sandt, J.D., Kolle, M., Dunkel, J., 2020. Topological mechanics of knots and tangles. Science 367 (6473), 71–75.

Wang, L.; Kim, Y.; Guo, C. F.; Zhao, X., Hard-magnetic elastica. *J Mech Phys Solids* **2020,** *142*, 104045.

Wang, L.; Zheng, D.; Harker, P.; Patel, A. B.; Guo, C. F.; Zhao, X., Evolutionary design of magnetic soft continuum robots. *Proceedings of the National Academy of Sciences* **2021,** *118* (21), e2021922118.

Weeger, O., Yeung, S.-K., Dunn, M.L., 2018. Fully isogeometric modeling and analysis of nonlinear 3D beams with spatially varying geometric and material parameters. Comput. Methods Appl. Mech. Eng. 342, 95–115.

Weeger, O., Narayanan, B., De Lorenzis, L., Kiendl, J., Dunn, M.L., 2017. An isogeometric collocation method for frictionless contact of Cosserat rods. Comput. Methods Appl. Mech. Eng. 321, 361–382.

Baek, C., Reis, P.M., 2019. Rigidity of hemispherical elastic gridshells under point load indentation. J. Mech. Phys. Solids 124, 411–426.

Baek, C., Sageman-Furnas, A.O., Jawed, M.K., Reis, P.M., 2018. Form finding in elastic gridshells. Proc. Natl. Acad. Sci. 115 (1), 75–80.

Yu, T.; Dreier, L.; Marmo, F.; Gabriele, S.; Parascho, S.; Adriaenssens, S., Numerical modeling of static equilibria and bifurcations in bigons and bigon rings. *J Mech Phys Solids* **2021,** *152*, 104459.

Ascher, U. M.; A Mattheij, R. M. M.; A Russell, R. D., *Numerical Solution of Boundary Value Problems for Ordinary Differential Equations.* Society for Industrial and Applied Mathematics: 1995.

Dankowicz, H.; Schilder, F., *Recipes for Continuation.* Society for Industrial and Applied Mathematics: 2013.

Dankowicz, H., Schilder, F., 2010. An extended continuation problem for bifurcation analysis in the presence of constraints. J. Comput. Nonlinear Dyn. 6 (3).

Weinitschke, H.J., 1985. On the calculation of limit and bifurcation points in stability problems of elastic shells. Int. J. Solids Struct. 21 (1), 79–95.

Eriksson, A., Pacoste, C., Zdunek, A., 1999. Numerical analysis of complex instability behaviour using incremental-iterative strategies. Comput. Methods Appl. Mech. Eng. 179 (3), 265–305.

Timoshenko, S.P., Goodier, J.N., 1951. Theory of elasticity. McGraw-Hill, New York.